



Technical University of Civil Engineering of Bucharest

Building Services Engineering Faculty

Doctoral School

RESEARCH REPORT 3

Experimental study of transpired solar collector prototypes for drying needs.

Ph.D. Student

Ing. Charles BERVILLE

Thesis supervisor

Conf. univ. dr. ing. Ilinca NASTASE

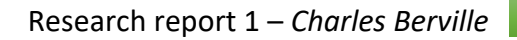
BUCHAREST

2021



Table of contents

1.	Introduc	tion	6
	1.1. Cor	ntext	6
	1.2. The	project & objectives	7
2.	Indoor e	xperimental study	9
	2.1. Mat	erial and methods	9
	2.1.1.	Experimental stand	9
	2.1.1.1	Indoor solar collector	9
	2.1.2.	Measuring device	10
	2.1.2.1	Thermocouples	10
	2.1.2.2	2. Flow Meter	11
	2.1.2.3	3. Ambient air parameters	13
	2.1.2.4	4. Camera IR	14
	2.1.2.5	5. Solar simulator	15
	2.1.3.	Methods	21
	2.2. Res	ults & Discussions	24
	2.2.1.	Continuous solar radiation.	24
	2.2.2.	Intermittent solar radiation	27
3.	Outdoor	experimental studies	29
	3.1. Mat	erial and methods	29
	3.1.1.	Measuring devices	29
	3.1.1.1	Outdoor solar radiation	29
	3.1.1.2	2. Wind velocity	29
	3.1.2.	Outdoor solar facades	30
	3.1.3.	Solar dryer	31
	3.1.4.	Governing equations	32
	3.2. Cor	trol strategies	33
	3.3. Res	ults & Discussions	34
	3.3.1.	Solar Façade lifetime issues	35
	3.3.2.	Thermal behaviours	35
	3.3.3.	Heating and energy production capacity	38
	3.3.4.	Simplified method for evaluating thermal performance TSC and DSTSC	42
4.	Conclusi	on and future works	43
5.	Dissemir	nation	44
	5.1. Aut	hor	44







List of figures

Figure 1.	Schematic c	liagram of the pi	roposed demons	trator			8
Figure	2.	Bucharest	Climate	Graph	in	Metric	Units,
		· ·	om/graph.php				
_			without back-pa		•		
•							
_			ge drive				
			r during an indoo				
Figure 8.	The FlowFin	ıder®mk2 used o	on false ceiling fo	or air flow mea	surement		13
_			vity of the absor	•	-		•
Figure 10). Distributio	n of 500 W halo	gen lamp radiati	on [19]			15
Figure 11	L. Arrangem	ent of the 500W	/ halogen lamps	for different of	distance be	etween the eda	ges of the
lamps [19	9]						16
_		_	en lamps				
Figure 13	8. Arrangeme	ent for a 8 halog	en lamps solar si	mulator with	D=26cm		17
Figure 14	l. Arrangeme	ent for a 8 halog	en lamps solar si	mulator with	D=10cm		17
Figure 15	. Measuren	nents of solar sir	nulator intensity	using a pyran	ometer		18
Figure 16	6. Distributio	n of the radiatio	n of solar simula	itor when H= 4	40cm and	D=10cm	19
Figure 17	7. Distributio	n of the radiation	n of solar simula	ator when H=	80cm and	D=10cm (left)	and when
H= 80cm	and D=26cn	n (right)					20
Figure 18	3. Temperat	ure distribution	across the exter	rnal surface o	f TSC at a	radiation of 5	70 W/m².
Measure	d temperatu	ires using infrare	ed camera: (left)	with fan off, (B) with far	n on	20
Figure 19). Thermoco	uple distribution	for DSTSC (left)	and TSC (right	t)		21
Figure 20). Thermoco	uple distribution	for the DSTSC (I	eft) and TSC (ı	right)		22
Figure 21	. Evolution	of the temperati	ire on the perfoi	rated plate for	the DSTS	C	23
Figure 22	2. IR camera	in front of the so	olar collector				23
_		•	ire for the TSC				
			ire on the perfoi				
Figure 25	i. Temperatı	ire difference be	etween ambient	and outlet air			25
_	•		etween ambient			_	
Figure 27	'. Temperatu	ire difference be	etween ambient	and outlet air	for TSC an	d DSTSC at 400)m³/h. 27
Figure 28	3. Temperati	ire difference be	etween ambient	and outlet air	for TSC an	d DSTSC at 500)m³/h. 28
Figure 29). Scheme of	the device for w	ind velocity and	wind directio	n		29
_		_	Solar Air Collecto				
_	_	-	ryer				
Figure 33	3. Solar façad	de after 2 years (left), new solar f	açade (right).			35
Figure 34	l. Variation o	of solar radiation	and the temper	ature of TSC,	DSTSC and	ambient air	36
Figure 35	5. Variation o	of solar radiation	and the temper	ature differen	ice (Δ T) of	TSC and DSTSC	2 37
Figure 36	5. Variation	of the temperat	ure difference (Δ T) of TSC an	nd DSTSC f	or an intermit	tent solar
	•						
_			of the temperat				
		•					
Figure 38	3. Variation o	of the heating ca	pacity and solar	radiation			39



Figure 39. Variation of the absorber plates' effectiveness and solar radiation from 09:00 to 17:00.	40
Figure 40. Variation of the solar collectors' efficiencies and solar radiation from 09:00 to 17:00	40
Figure 41. Effect of the wind velocity on the solar collectors' efficiencies	41
Figure 42. Zoom on the effect of the wind velocity on the solar collectors' efficiencies	41
Figure 43. Evolution of the ΔT in function of the solar radiation at 450m 3 /h	42
Figure 44. Experimental stand for TES investigations	43



List of tables

Table 1. Technical features of Calibration thermostats	11
Table 2. Specifications of the flow meter	12
Table 3. Indoor Air Quality probes specifications	13
Table 4. IR camera specifications	14
Table 5. Technical data of the Star Pyranometer Type FLA628S	18
Table 6. From 1:30 to 2:15	26
Table 7. Heat and energy capacity at 400m ³ /h	28
Table 8. Heat and energy capacity at 500m ³ /h	28
Table 9. Solar radiation composition	29
Table 10. Technical data for Wind Velocity Sensor Type FVA615-2	30
Table 11. Technical data, Wind Direction Sensor Type FVA614	30
Table 12. Power supply unit specifications	31
Table 13. Minimum and maximum airflow values	35
Table 14 From 09:00 to 17:00	39



1. Introduction

1.1. Context

The building sector is the biggest energy consumer and greenhouse gas emissions contributor in the world. It is still representing 36% of the final global energy consumption and 40% of the greenhouse gas emissions, being critical to reduce the energy consumption of the building sector in the coming years.

Since the emergence of skyscrapers during the 20th century architects and building designers focused on high rise building made of concrete and metal structure wrapped in glass facades. These shiny and high energy consumption buildings are no longer in accordance with the standards and needs of our times.

Since 2010, the European Union has established policies including Energy Performance of Buildings Directive 2010/31/EU (EPBD) and Energy Efficiency Directive 2012/27/EU (EED) to improve the building sector in European Union. These policies have been strengthened first in 2018 (2018/844/EU) in the establishment of the Clean energy for all Europeans package to be in accordance with the Paris Agreement and then in December 2019 during the presentation of the European Green Deal. All these directives and policies are made to improve the energy efficiency and to decarbonize the building sector until 2050. By the end of 2020 early 2021 all new building should be Nearly Zero-Energy Buildings (NZEB) and in the near future to achieve Positive Energy Buildings (PEB) [1].

In order to achieve all these objectives new energy systems should be proposed and building architectures should be reconsidered. Some of the solutions are anchored in the building itself, and from these our attention is focused on the building envelope/facade. Building facades are a huge source of energy which for a long time have been forgotten in building conception. Building facades can harness large amounts of energy from the sun [2]. In recent years, new building facades concepts and active building envelope systems have emerged [3] such as ventilated, Building-Integrated Solar Thermal systems [4, 5], photovoltaic [6] or algae bio-reactive facades [7, 8]. Among these, ventilated or solar air façades have the advantage of being inexpensive and easy to integrate in new building architectures or retrofit. The adaptability of system for existent or new buildings is an important manner to introduce a new product in the building sector. In order to enlighten this issue experts [9] from 14 countries presented a panel of initiatives and guidelines to integrate solar energy in architecture. This report further noted the importance of the design, colour, material, and size for the harmonious integration of solar energy systems in architecture.

In this momentum of initiatives and advancements regarding solar energy and architecture a team from the university of Brasov developed a new geometry of solar thermal collector [10] combining architectural aspect and energy efficiency. This novel solar thermal collector has smaller surface and a trapeze shape instead of rectangular shape in order to facilitate the integration in building. A two-year experimental study [11] has shown similar performance for the prototype of trapeze flat plate solar collector comparative to a commercial rectangular collector integrated in a building block façade.

Cristofari et al. conducted a refurbishment study [12] with two novel patented integrated solar thermal system for a residential building. The first solar thermal system is a flat solar water collector



and in second system is an air heater integrated as a window. Results have shown that the patented solar water collector can reduce the energy consumption for hot water by 45% and the air heater can provide 47% of the energy needs for space heating.

Building refurbishment using sandwich panel is a common fact, however they are not the best option regarding the environmental impact. Elguezabal et al. proposed new design [13] of sandwich panel with integrated thermal collector, this new alternative can increase the interest of sandwich panel for NZEB refurbishment. Results have shown an efficiency of 0.34 - 0.47 and an energy loss factor between 4.85 and 7.5.

Ventilated facades such as Transpired Solar Collectors have the advantage to insulate the building envelope and to provide heated air for the building heating needs. Thus, TSC can reduce the building energy needs and provide a renewable energy source for air heating.

A common question is why "why don't you put glazing on the collector to optimize thermal performance?". The answer is a frequent question from architects related by J. C. Hollick in the premises of research on UTSC collectors, "can you get rid of the glazing?". The use of glazing in the conception of solar air heaters makes the implementation in the building complicated regarding the handling and the additional load on the façade, especially for large area building.

In this wide group of Building-Integrated Solar Thermal systems we find the Transpired Solar Collectors (TSC). TSC can be glazed (GTSC) or unglazed (UTSC), they are usually implemented on large scale buildings, such as industrial, office or multi-families residential building for ventilation and space heating during cold period. This kind of solar air collector has the advantage of being cheap and easy to integrate for a building retrofit.

Transpired solar collectors have been widely studied during the last 30 years by experimental, mathematical, and numerical approaches. Computational Fluid Dynamics (CFD) studies on UTSC started in the late 90s with a 2D simulation conducted by Gunnewiek et al. [14]. This study has shown the importance of the heat transfer at the back of the perforated absorber plate. In another study [15], they upgraded their numerical model by adding the effect of the wind. Conclusions of this paper are very useful, indeed, Gunnewiek et al. demonstrated that a suction velocity should be maintain above 0.0125 to 0.039 m/s depending on the building type to avoid reverse flow. Another solution proposed by Gunnewiek et al. to mitigate the negative effect of the wind speed is to avoid perforations on the upper part of the collector.

In 2001, an important physical phenomenon for UTSC has been described by [16], they determined that total heat transfer is distributed in different parts of the absorber plate. The air temperature rise is distributed as such: 62% on the front, 28% in the hole and 10% on the back of the plate.

Then in 2002 Gawlik and Kutscher [17] continued the CFD study on the effect of the wind speed, suction velocity, and absorber plate shape. In the same year [18], they conducted a comparative numerical and experimental study of two different material type of absorber plate, plastic and aluminum, they concluded that the thermal conductivity of the absorber plate has no significant effect on the thermal performance of the UTSC.

1.2. The project & objectives



The overall goal of the project is to endorse the circular economy concept, helping local urban agriculture development for a sustainable food future. The project aims to prove that the renewable energy sources used for heating the buildings during the cold period can successfully also address the energy needs of urban farming, in the process of food preservation during the cropping period, closing the loop. Thus, the symbiotic system of the building, as a shelter and as a food source, integrates seamlessly in sustainable urban communities.

The scope of the project is to develop an experimental demonstrator to prove the all year-round functionality and efficiency of the concept building adaptive solar energy system, integrating cascaded Phase Change Materials, for passive air heating and food drying purposes.

The adaptive solar system will lead to two main objectives: providing the pre-heated building fresh air during the cold period and providing heated air for drying process of the crop resulted from local urban farming during the warm period.

Transpired solar collectors (TSC) are usually implemented on large scale buildings, such as industrial, office or multi-families residential building for ventilation and space heating during cold period and during warmer period the heated air from the system is usually by-passed. This observation has led us to the concept of a solar dryer using the lost energy of the TSC during summertime. The purpose is to prove the possibility of solar façades for multipurpose drying needs in order to value them during summertime. This project proves a technical application of energy recovery of the wasted heat generated by energy usage during summertime, also contributing to the heat island effect.

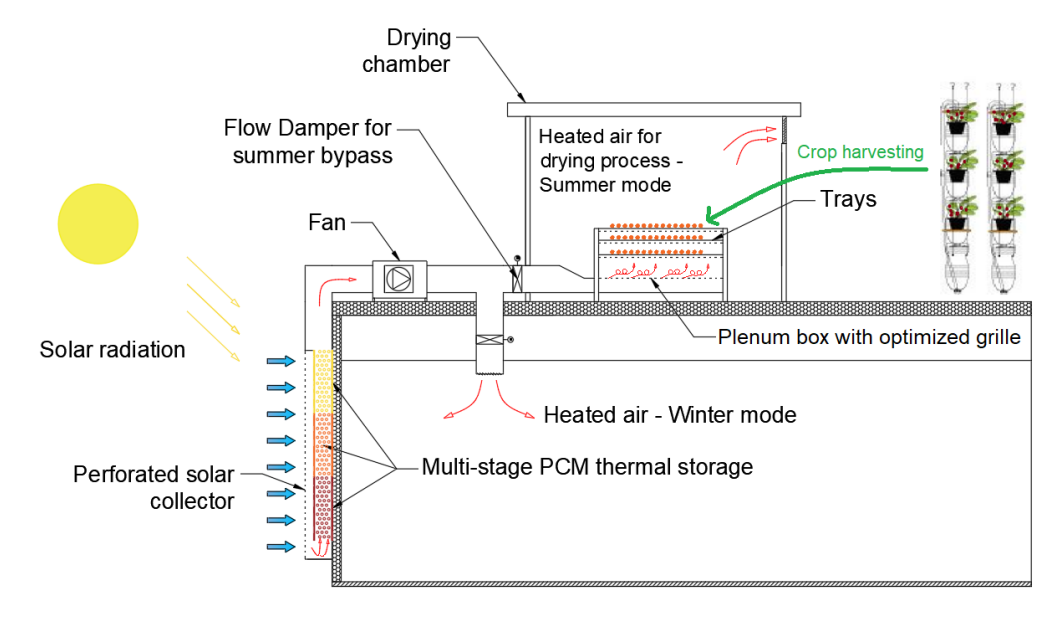


Figure 1. Schematic diagram of the proposed demonstrator

The aim of this report is to experimentally analyses the thermal behavior and performance of a prototype of double skin transpired solar air collector during summertime. The outcome of the report is to determine the potential of solar façades for drying operations.

Experiments have been done at the Faculty of Building Services in the city of Bucharest, Romania. Bucharest has a humid continental climate with hot summer (base temperature = 35,3°C, humidity =35%) and cold winter (base temperature = -15°C). Figure 2 presents the climate parameters for the city of Bucharest.



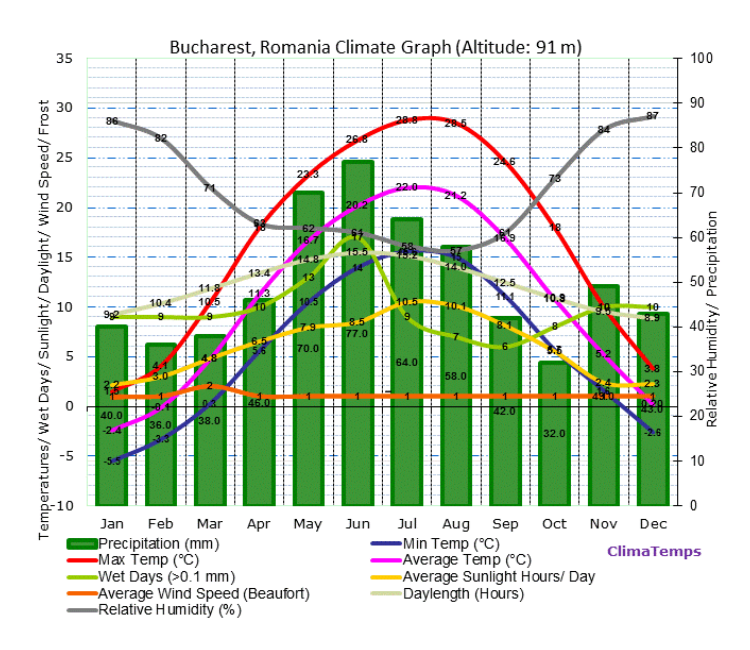


Figure 2. Bucharest Climate Graph in Metric Units, http://www.bucharest.climatemps.com/graph.php

2. Indoor experimental study

2.1. Material and methods

2.1.1. Experimental stand

2.1.1.1.Indoor solar collector

The first part of our experimental studies concerns the analyses of Transpired Solar Collectors and Double Skin Transpired Solar Collectors in indoor condition. We constructed an indoor experimental stand, presented in the Figure 3, consisting in a double skin transpired solar air collector, rigid and flexible circular duct, axial fan, and solar simulator based on 8 halogen lamps of 500W.







Figure 3. Indoor experimental stand

Wooden beams have been added inside the solar collector to support the second metal plate used as a back-pass, Figure 4.







Figure 4. Interior view of the DSTSC, without back-pass, with back-pass and front air gap, from left to right.

The solar collector has been connected to a fan via a flexible duct. The fan is connected to variable voltage drive, Varionys® M presented in the Figure 5, to work at the right operating point. With a variable voltage drive, we can easily set the flow rate we need for each experimental set-up.



Figure 5. Axial fan with variable voltage drive

2.1.2. Measuring device

2.1.2.1.Thermocouples

Initially, we used a thermocouple welder to weld thermocouple junctions. We used a professional thermocouple welder based on a heated resistance, as shown in a the Figure 6.





Figure 6. Thermocouple welding.

When thermocouples are linked via junction, we then calibrate/correct them. The calibration/correction was performed with thermostatic bath from 0 to 80°C as recommended by the supplier. To calibrate thermocouples, we used two different references for the temperature, one from the integrated temperature sensor of the thermostatic bath – LAUDA Ecoline Staredition RE 312 J - and another from a digital platinum resistance thermometer (LAUDA DigiCal DCS 2 - Pt100 Kl. B1/3 DIN sheath resistance probe in 4-conductor).

 Working temperature range
 °C
 -30 to 200
 -200 to 450

 Temperature stability
 ±K
 0.01

 Resolution of indication
 °C
 0.05/0.01
 -200...200: 0.01 > 200: 0.1

Table 1. Technical features of Calibration thermostats

For calibration/correction, thermocouple NiCr-Ni class 2 with PVC Insulation and operating temperature from -10 to +105 °C were connected to an ALMEMO® connector wired to a data logger Albhorn 710. The data logger Albhorn 710 is useful to achieve maximum measuring accuracy, indeed the zero-point of the sensors can be corrected when the temperature in the bath is a 0°C. Then, by entering a setpoint the correction value will be automatically calculated and stored in the sensor ALMEMO® connector wired to a data logger.

2.1.2.2.Flow Meter

The air flow determination has been realized with an flow meter, FlowFinder mk2, which is fully zero pressure compensated in the range 10 to 550 m m3/h and has a calculated compensation up to 850 m3/h. Table 2 shows the specification of the air flow meter, FlowFinder mk2.



Table 2	Speci	fications o	f the	flow meter

Air flow range (supply and exhaust)	10 to 850 m³/h
Air temperature range	-20 to +80°C
Uncertainty	3% of the reading, with a minimum of 3 m ³ /h
Repeatability	better than 1%, with a minimum of 3 m ³ /h
Resolution	1 m³/h, 0.1cfm, 0.1l/s
RV range	0100%

The air flow meter should be placed perpendicular to the air flow and carefully manipulated during measurements to correctly determine the air flow value. Additionally, a straight hood can be used to facilitate and improve the accuracy of the measurement, as shown in the Figure 7. Every time, we repeat the measurement 2 or 3 times shortly after each other to lower the uncertainty.



Figure 7. Utilization of the flow meter during an indoor experiment

We can notice in Figure 7 that polystyrene plates have been used in front of the hood. These plates are used to avoid the air to escape or by-pass the flow meter, using them we make the measurements more airtight. Usually, this kind of flow meter is used to measure the air flow passing through air diffusers located on false ceiling, as shown in the Figure 8.





Figure 8. The FlowFinder®mk2 used on false ceiling for air flow measurement

2.1.2.3. Ambient air parameters

During all experiments the ambient air quality parameters have been measured. The ambient air parameters, such as the temperature, humidity and pressure are important, because they influence the behavior and functioning of the major part of the devices, even more, some device cannot work outside certain range.

For air quality parameters the universal IAQ instrument Testo 400 has been used. The Testo 400 can measure all IAQ-related parameters: Flow, temperature, humidity, pressure, illuminance, radiant heat, turbulence, CO_2 and CO. In our case, we used a turbulence probe with fixed cable to measure the air temperature, air velocity and pressure. The specificities of both probes are shown in Table

Probe type Measuring Resolution **Accuracy** range **Turbulence** 0 to +5 $\pm (0.03 \text{ m/s})$ $0.01 \, \text{m/s}$ probe m/s + 4% of 0.1 °C m.v.) 0 to +50 0.1 hPa °C (0 to 5 m/s)700 to ±0.5 °C 1100 hPa ±3 hPa **Humidity** / 0 to 100% ±2% RH (5 0.1% RH **Temperature** RHto 90% RH) 0.1 °C probe -20 to +70 ±0.5 °C °C

Table 3. Indoor Air Quality probes specifications



Measuring devices are usually calibrated by authorized company, nevertheless we compared the measurements of the temperature of both probes with another temperature probe, Lauda DigiCel DCS 2, to check the correctness of the calibration. Temperatures provided by the three probes are quite similar, we could observe a difference of +/-0.4°C between the three sensors, we considered them calibrated and accurate as they are in their range of accuracy of +/-0.5°C

2.1.2.4.Camera IR

An infrared or thermographic camera captures infrared radiation emitted by bodies. Infrared radiation or heat waves emitted by bodies vary according to their temperature. Thus, IR cameras make it possible to determine the temperature of a body quantitatively. It is similar to a camera that captures visible lights, from about 380 to about 750 nanometers, an IR camera captures infrared radiation with wavelengths between $1\mu m$ to $14\mu m$.

Table 4 presents the infrared camera used in the laboratory, a FLIR E40.

Measuring range

-20°C to +120°C (-4°F to +248°F)
0°C to +650°C (+32°F to +1202°F)

of reading

Table 4. IR camera specifications

The first step before using the infrared camera is to establish a reference temperature that should be manually set or captured from any measurement function. We captured (Figure 9) the reference temperature from a thermocouple NiCr-Ni class 2 with PVC Insulation and operating temperature from -10 to +105 °C connected to an ALMEMO® connector wired to a data logger Albhorn 710.

Parameters for black coated aluminum perforated plate:

Emissivity = 0.99-0.98



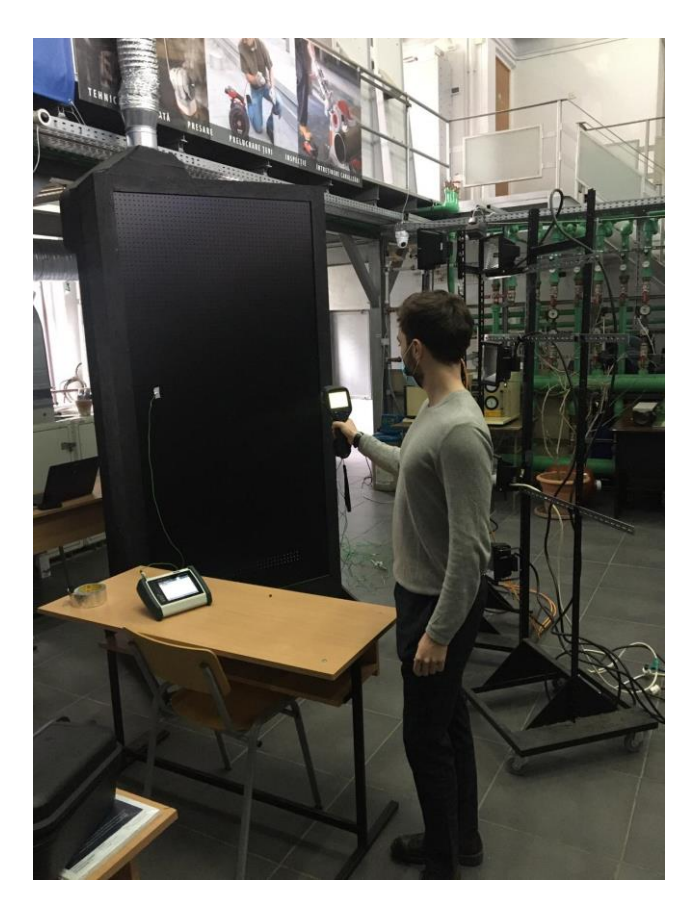


Figure 9. Measurement of the emissivity of the absorber plate using IR camera and thermocouples.

2.1.2.5. Solar simulator

It seems that best arrangement for solar simulator based on halogen lamps have been proposed by Moria et al. [19]. An issue often encountered when designing a solar simulator based on halogen lamp is non-uniform distribution of the radiation. Figure 10 shows the radiation distribution for one 500W halogen lamp, we can notice a huge variation of the radiation when we move away from the luminous focus of the lamp, especially when we are at 10cm of the lamp (H=10cm). Thus, it is complicated to combine high radiation intensity and uniformity. They find that the optimal irradiance is produced when lamps are distanced with 10cm, Figure 11. Their solar simulator can produce an irradiance between 200 W/m² and 1200W/m² with 8 halogen lamps of 500W each.

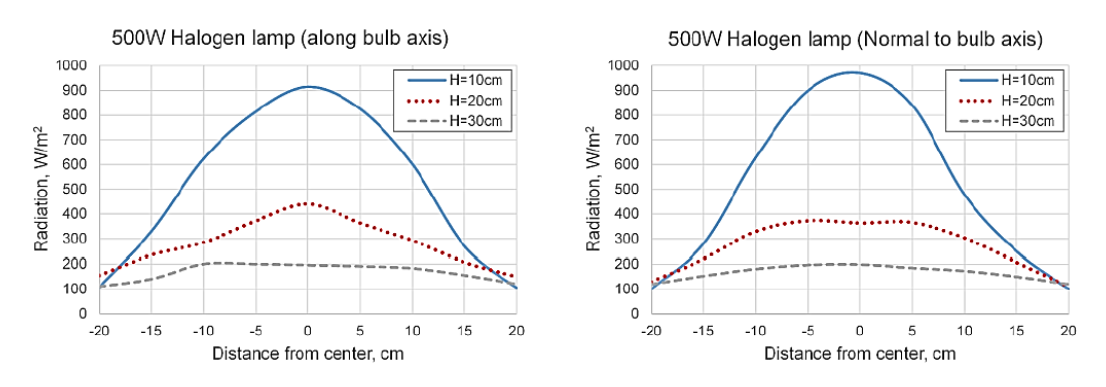


Figure 10. Distribution of 500 W halogen lamp radiation [19]



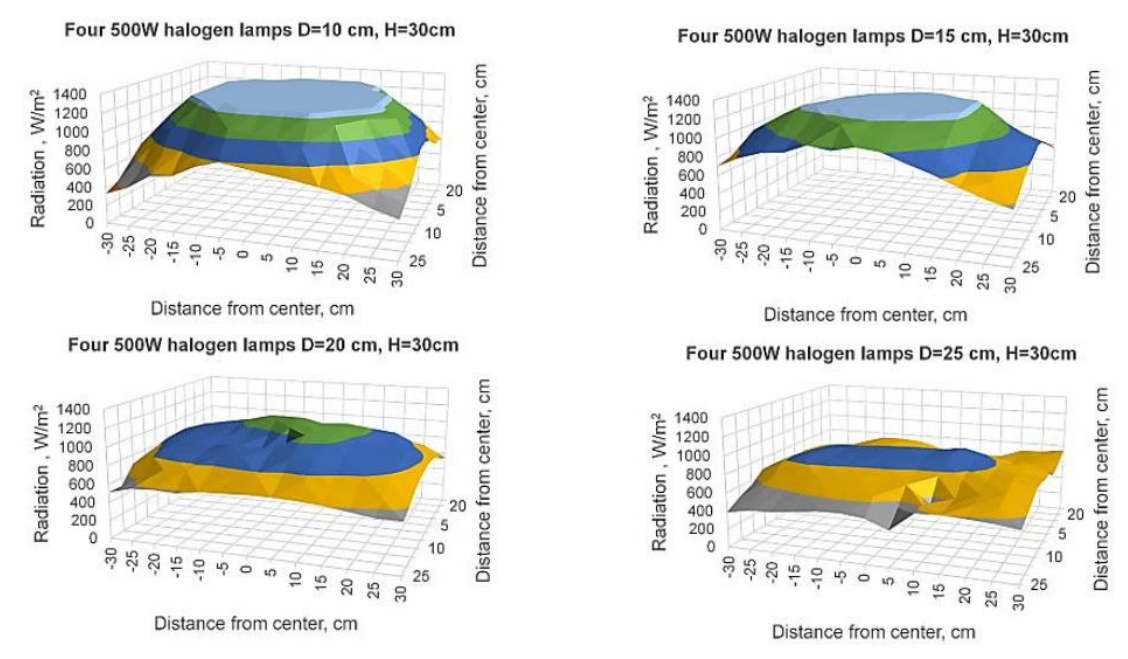


Figure 11. Arrangement of the 500W halogen lamps for different distance between the edges of the lamps [19]

According to our bibliographic research the number of lamps for a 2m² plate would be 21 to 32 lamps and the ideal arrangement would be as follows:

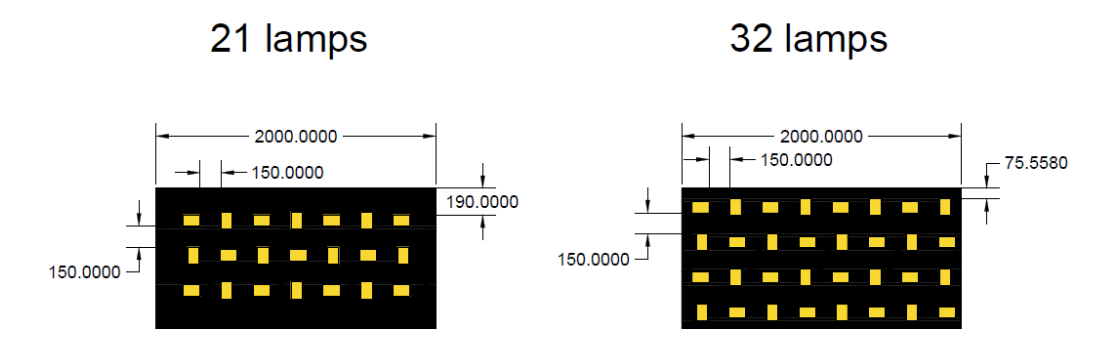


Figure 12. Ideal distribution of halogen lamps

However, the installation of so many halogen lamps is complicated and difficult to achieve for two reasons: In on, it requires enormous electrical power, from 10,5 to 16 kW. Secondly, the heat given off by the halogen lamps by the Joule effect will bias the total power delivered by the solar simulator. This is why we decided to build a solar simulator composed of 8 halogen lamps for technical reasons, we do not have a powerful enough electrical panel in the laboratory and we also do not have a ventilation and air conditioning system powerful enough to mitigate the temperature released by a solar simulator made up of more than 8 lamps.

We investiguated different arrangement for our 8 lamps solar simulator,



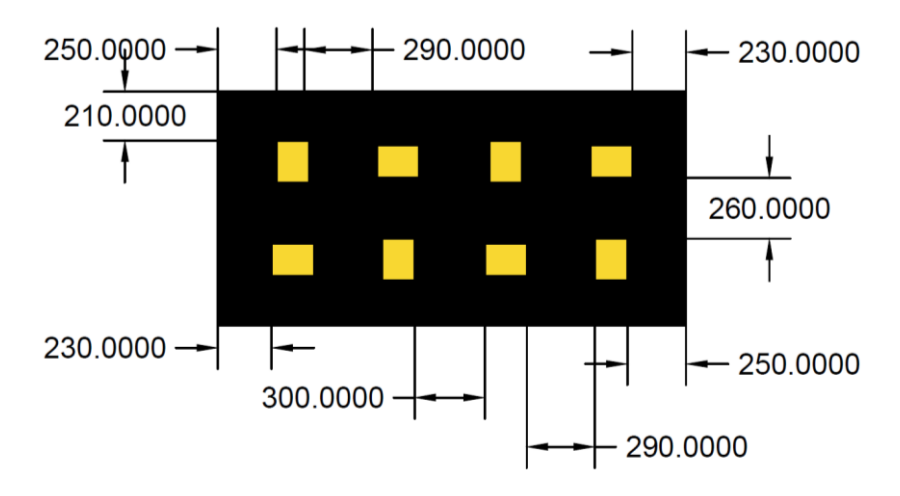


Figure 13. Arrangement for a 8 halogen lamps solar simulator with D=26cm

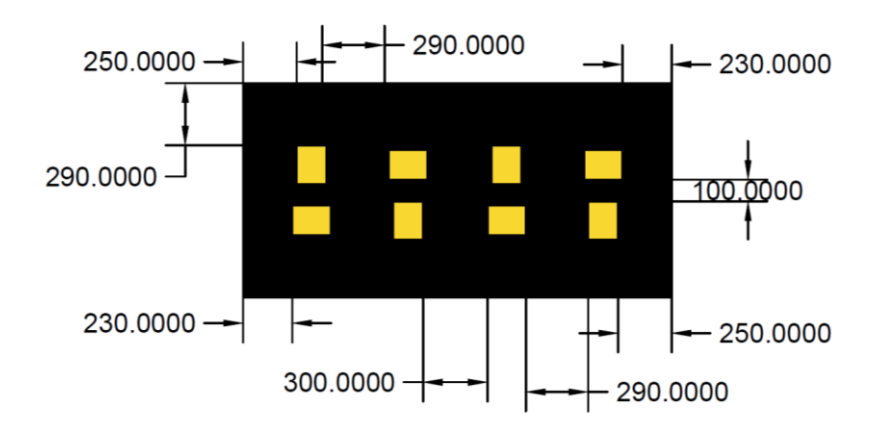


Figure 14. Arrangement for a 8 halogen lamps solar simulator with D=10cm

To determine the average global radiation (diffuse + direct) over the entire 2m² perforated plate we carried out measurements using a pyranometer for 30 points over the extent of the plate. Figure 15 shows the solar simulator, the pyranometer placed on a rack and connected to a data logger (ALMEMO 710). For every measurement we let the pyranometer in a fix position to determine the exact value for a point.







Figure 15. Measurements of solar simulator intensity using a pyranometer

Our pyranometer, Star Pyranometer Type FLA628S (Table 5), is measuring the global radiation independently from ambient temperature with an uncertainty of +/- 3% and a resolution of 0.1W/m^2 . Our first uncertainty was about the suitability of the pyrometer for determining the radiation of an Indoor Solar Simulator based on Halogen lamps, but the technical service department of Ahlborn, the supplier of the pyranometer, confirmed to us that the star pyranometer has an excellent wide wavelength range up to 3 μ m and should be suitable for our indoor investigations. Then, our second uncertainty was about the orientation of the pyranometer to measure the solar radiation on a vertical wall, if we should fix the pyranometer on the facade, vertically or horizontally. This question was consistent for both indoor and outdoor test. The conclusion is, to measure the radiation that affects the wall, it is better to install the pyranometer parallel to the wall (vertical). It will of course also measure radiation that comes nearly vertically and won't be absorbed by the wall but it is of course better than the horizontal position.

Table 5. Technical data of the Star Pyranometer Type FLA628S

Measuring range	0 to 1500W/m ²
Resolution	0.1W/m ²
Spectral range	0.3 to 3μm
Output	15μV/Wm-2
Impedance	35Ω
Operative range	−40 to +60°C
Accuracy	cosine effect: <3% of measured value
	(0 to 80° inclination)
	azimuth effect: < 3%
	temperature influence: < 1% (-20 to +40°C)



Nominal temperature	22°C ±2°C
Linearity	<0.5% (0.5 to 1330W/m2)
Settling time	25 second

We carried out a mapping based on the experimental value obtained previously. Tecplot 360 has been used as post processing tools to analyze experimental data. A mapping or a plotting the contour of experimental data is very helpful for us, we can easily visualize and analyze the best setting for our solar simulator. We tried different settings varying the distance between the lamps and between the solar simulator and the solar collector absorber. Figure 16 shows the distribution of the radiation of our solar simulator for a first settings based on our literature review, when H= 40cm and D=10cm, a high variation of the intensity of the radiation is noticeable, from 150W/m² in the corners of the absorber plate to 900 W/m² in the middle part of the absorber. We speculate that this might be due to a too short distance between the lamps and the absorber. This setting has not met our expectations, thus, we tried to increase the distance between the lamps and the absorber.

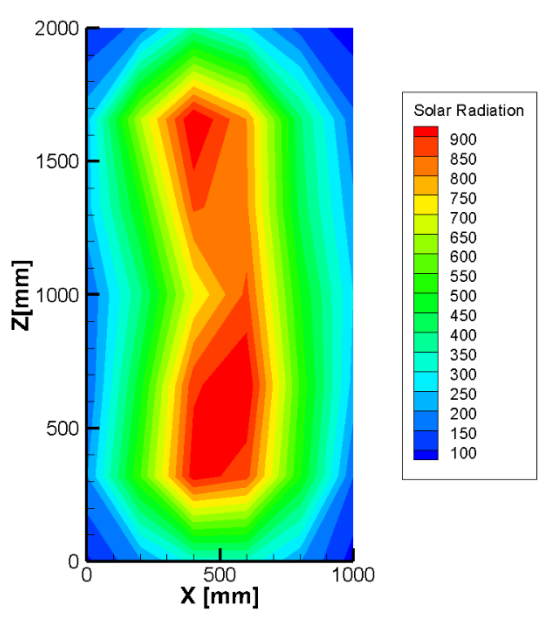


Figure 16. Distribution of the radiation of solar simulator when H= 40cm and D=10cm

Figure 17 shows the distribution of the radiation for two settings when H= 80cm and D=10cm (left) and when H= 80cm and D=26cm (right). We first tried to increase the distance between the solar simulator and the absorber from 40cm to 80cm, the results shown that it has a good influence on the uniformity as speculated previously. Another setting, H= 80cm and D=26cm (right), has been attempted, the objective was the make the spectrum more uniform in when increasing the distance between lamps, from 10cm to 26cm, however, the results were not consistent, it just distorted the radiation spectrum. The conclusion is that, both settings are still non-uniform, however, the setting on the left is more acceptable.



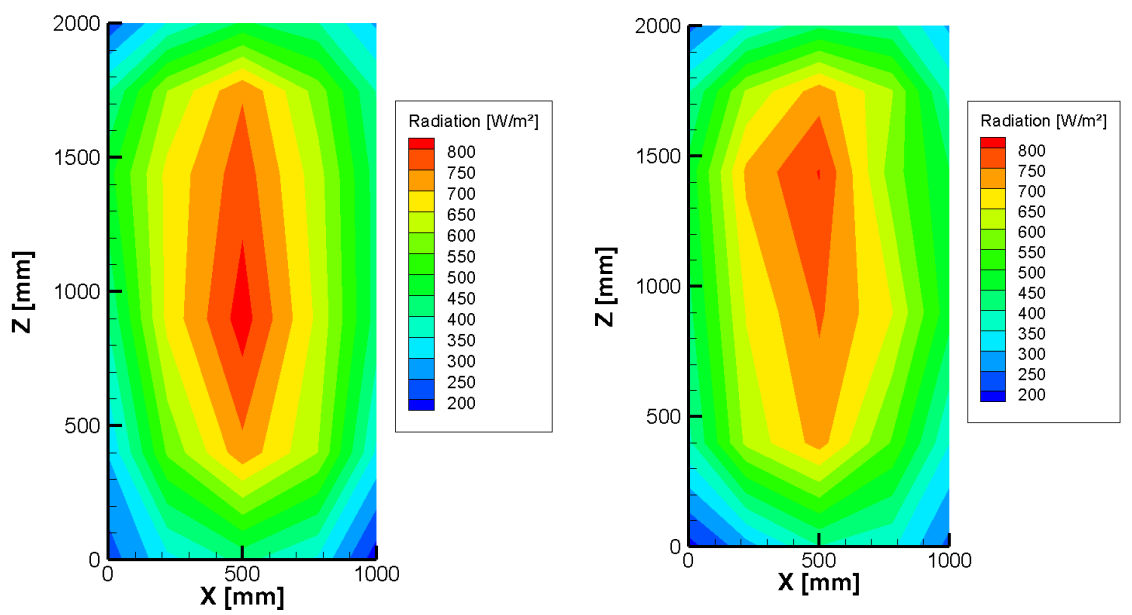


Figure 17. Distribution of the radiation of solar simulator when H= 80cm and D=10cm (left) and when H= 80cm and D=26cm (right).

Using Tecplot we determined a global medium radiation on the plate of 570 W/m^2 for the case when H= 80cm and D=10cm, Figure 17.

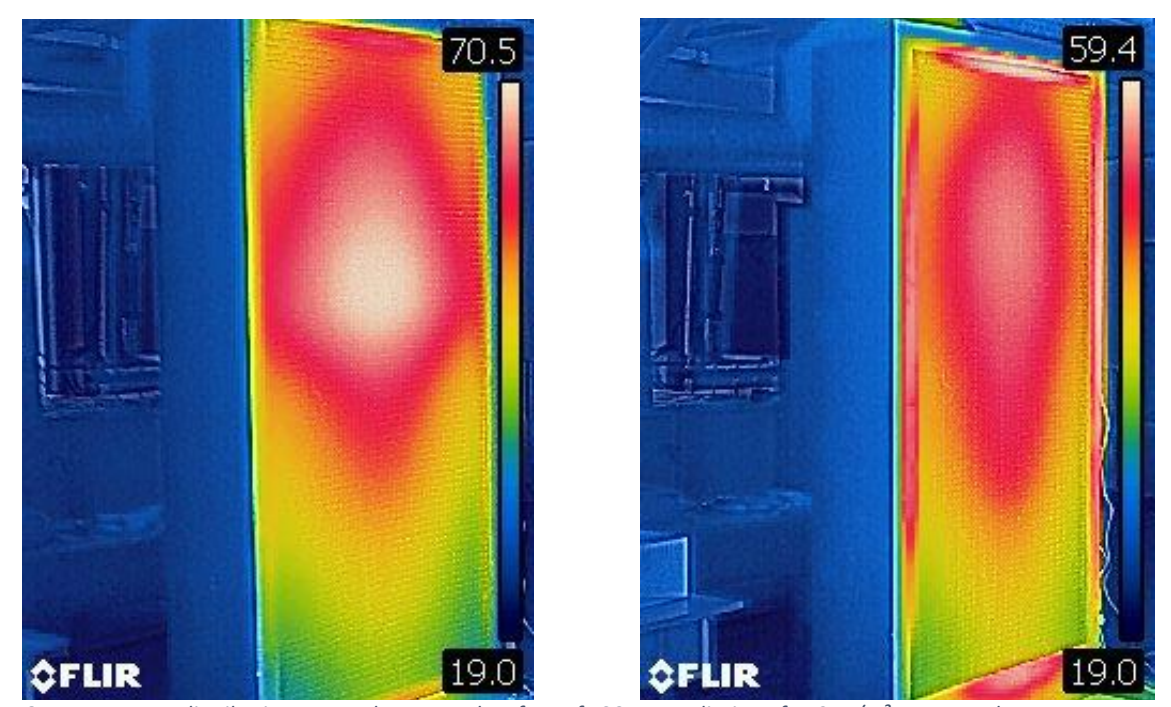


Figure 18. Temperature distribution across the external surface of TSC at a radiation of 570 W/m². Measured temperatures using infrared camera: (left) with fan off, (B) with fan on.

We can notice that the distribution of the simulated solar radiation (Figure 17) is not similar to the temperature distribution across the external surface of the TSC when the fan is not functional (Figure 18.A.). At first, we thought that the radiation distribution and the temperature distribution would be similar when the fan was turned off. From this standpoint, we considered that this difference is due



to the thermal stratification, thus, the temperature on the solar collector is higher in the upper part when the fan is turned off. The temperature distribution obtained when the fan is turned on (Figure 18.B.), at a flow rate of 400m³/h, confirm the speculation regarding the thermal stratification. Indeed, when the fan is turned on, the temperature distribution on the perforated absorber plate become more homogeneous and similar to the distribution of radiation showed in the Figure 17.

2.1.3. *Methods*

The main focus of the experiments was to analyze the thermal behavior of the Transpired Solar Collector and Double Skin Transpired Solar Collector. To monitor the temperature during the experiments we installed 15 thermocouples distributed over each solar collector, Figure 19 and Figure 20. We can notice in both figures that we have evenly distributed the sensors to capture a global thermography of both collectors. 5 thermocouples (red) have been placed on the perforated absorber plate and one (green) at the outlet for both collectors. 6 thermocouples (yellow) have been placed in the back-pass air channel of the DSTSC along with 3 thermocouples (orange) on the aluminum back-pass. 6 thermocouples (yellow) have been placed inside the TSC along with 2 thermocouples (orange) on the back plate. All these sensors have been used to make the comparison possible between the two collectors.



Figure 19. Thermocouple distribution for DSTSC (left) and TSC (right)







Figure 20. Thermocouple distribution for the DSTSC (left) and TSC (right)

Measurement of ambient parameters related to Indoor Air Quality via the universal measuring device Testo 400. This device, depending on the probes connected, allows the measurement of the following parameters: flow rate, temperature, humidity, pressure, lighting, heat radiant, turbulence, CO_2 and CO.

For our experiment, we used a turbulence probe for the measurement of temperature, air speed as well as pressure.

We turn on the solar simulator consisting of 8 halogen lamps of 500W each. The solar simulator is placed at 0.8m from the solar collector, this allows to obtain an average radiation on the absorber of 800-580 W/m². The solar simulator has been turned on for 1h40min to determine when the maximum temperatures are reached. The Figure 21 shows the evolution of temperatures in the DSTSC, this allows us to determine the stabilization time between each action to optimize the total time of the experiment. We can notice that after 20-30min the temperatures measured in the collector stabilize, especially the temperature of the perforated absorber plate. We therefore turn on the fan placed upstream of the collector on a circular duct. The fan is connected to a voltage regulator which allows us to adjust the flow precisely in the desired level. Depending on the flow rate chosen, the temperatures stabilize in the system between 15 and 30min.



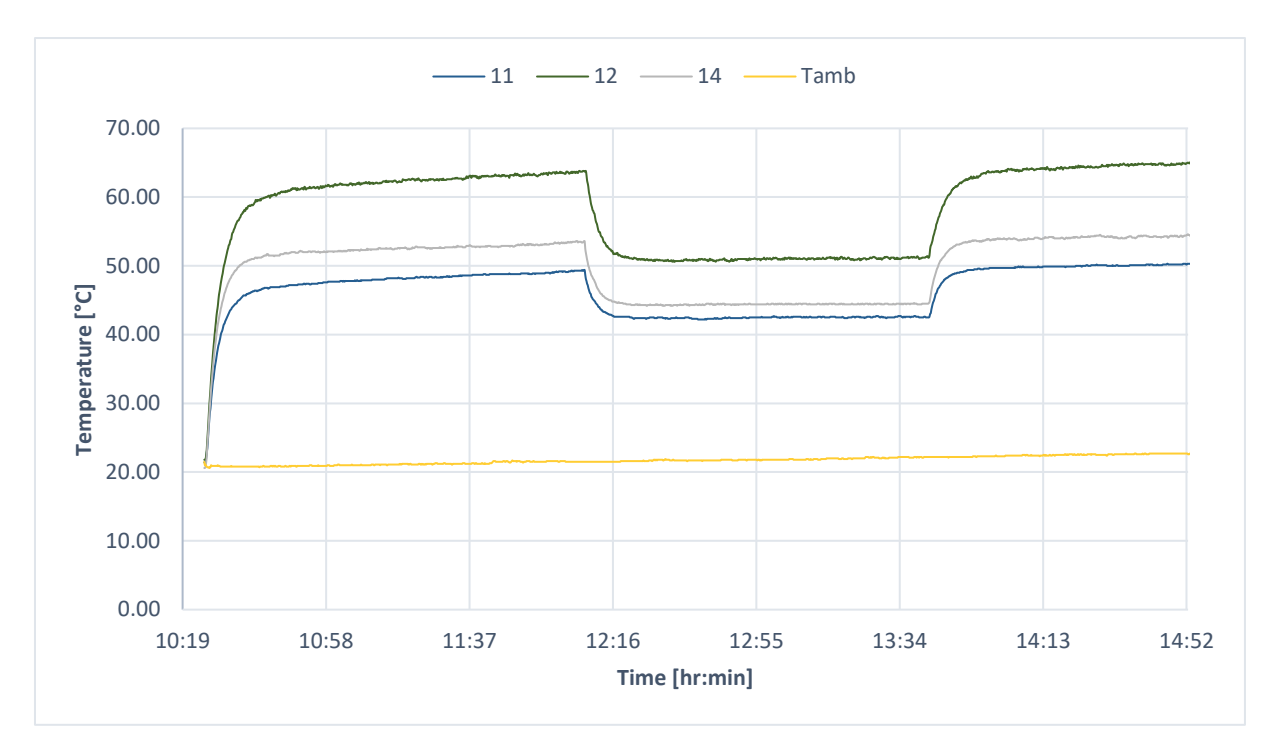


Figure 21. Evolution of the temperature on the perforated plate for the DSTSC

In parallel, we place the infrared thermal camera in front of the collector (Figure 22) to observe the evolution of temperatures on the absorber, either via a compilation of photographs or via a video. This allows us to check the temperature stability on the collector via another measuring device.

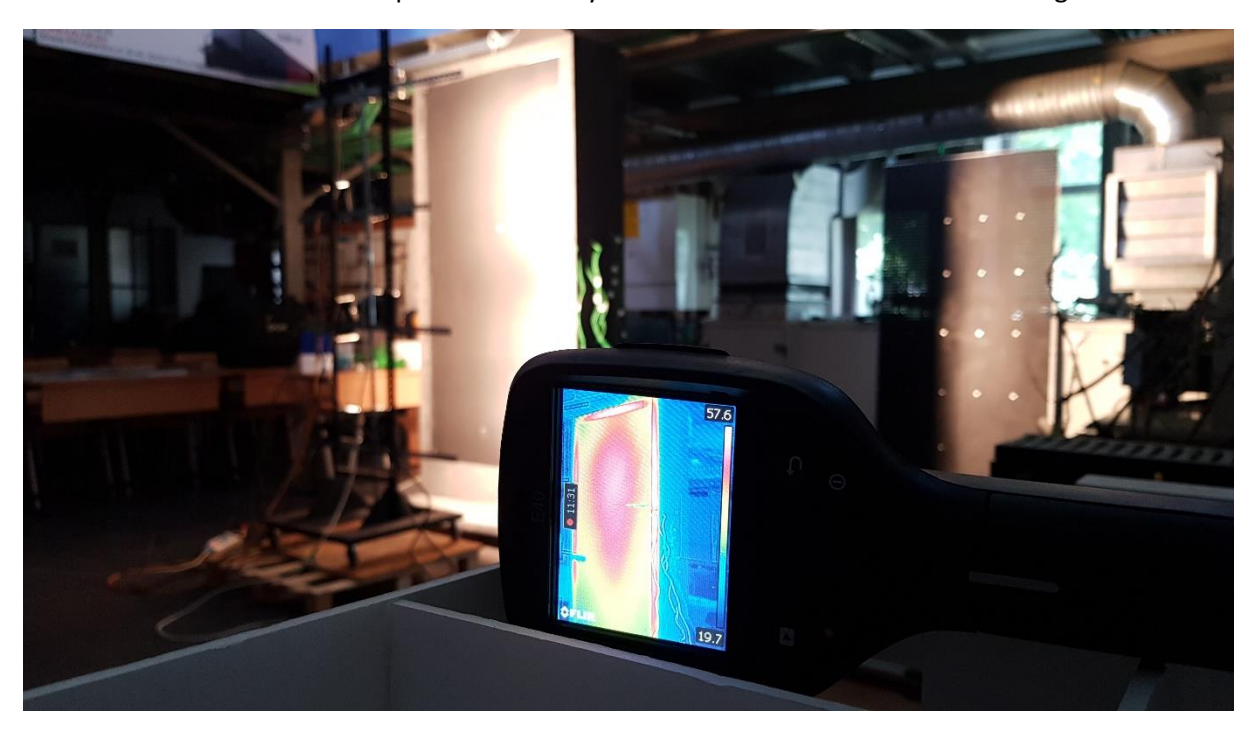


Figure 22. IR camera in front of the solar collector

Once the temperatures are stable when the fan is on, we turn off the fan while leaving the camera, probes, and solar simulator on. We are therefore observing a rise in temperatures until the temperatures stabilize again. After the experiments are over, we extract the data from the IR thermal camera and the data logger which compiled all the temperatures measured by the thermocouples.



2.2. Results & Discussions

2.2.1. Continuous solar radiation

We simulated the heating of the solar collector via a solar simulator composed of 8 halogen lamps of 500W over a period of 1h30min, then we started the axial fan with a flow of 500m³/h. This operation mode has been implanted for both collectors. Thermocouple number 13 was not working during the experiment with the TSC so we replace it by the thermocouple 6.

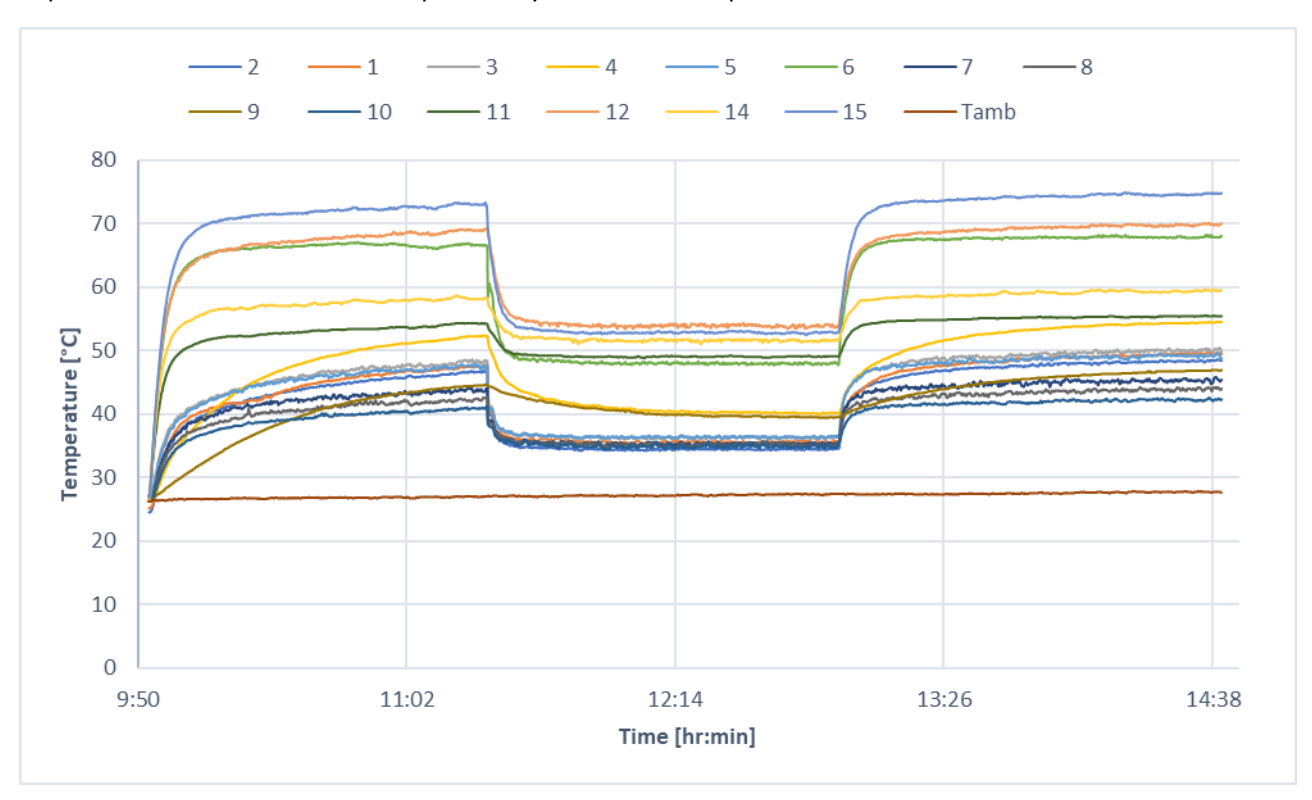


Figure 23. Evolution of the temperature for the TSC



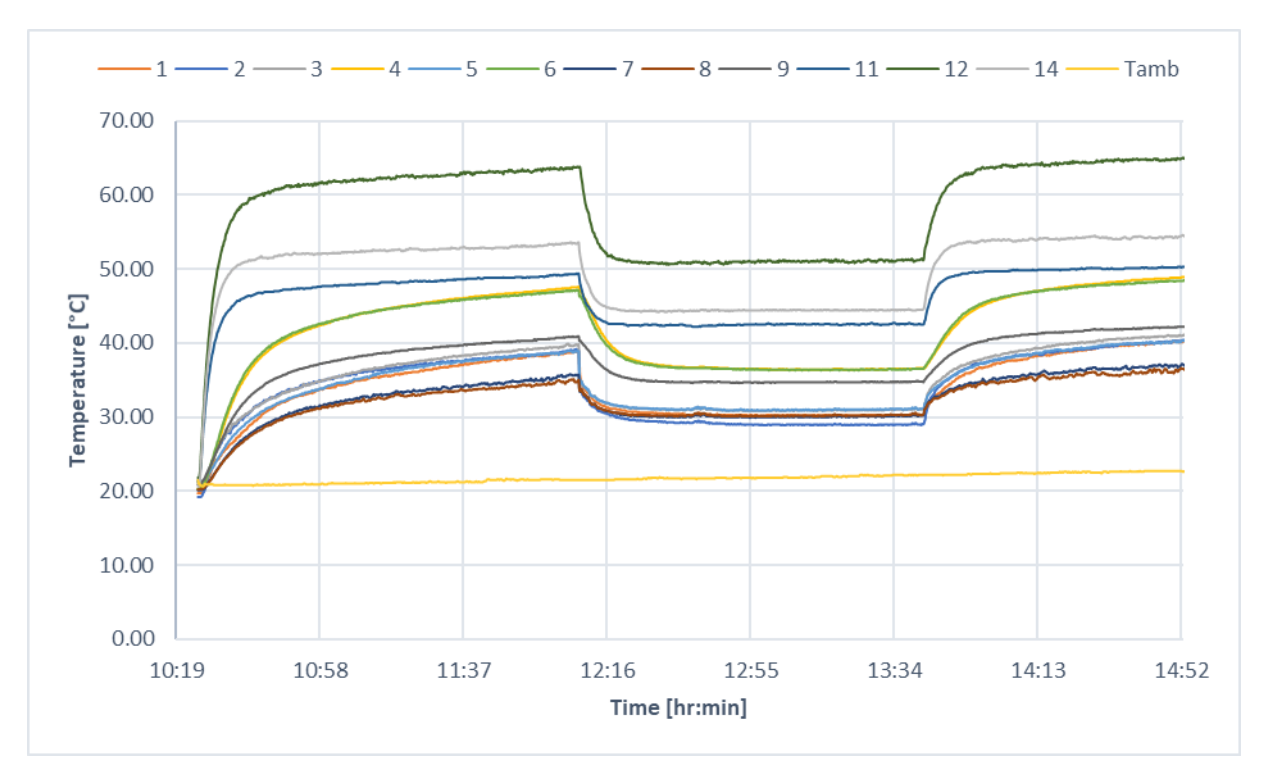


Figure 24. Evolution of the temperature on the perforated plate for the DSTSC

Figure 25 shows the temperature difference between the ambient and outlet air for both collectors, TSC and DSTSC. We can observe that the DSTSC undergoes a less sudden temperature drop than the TSC.

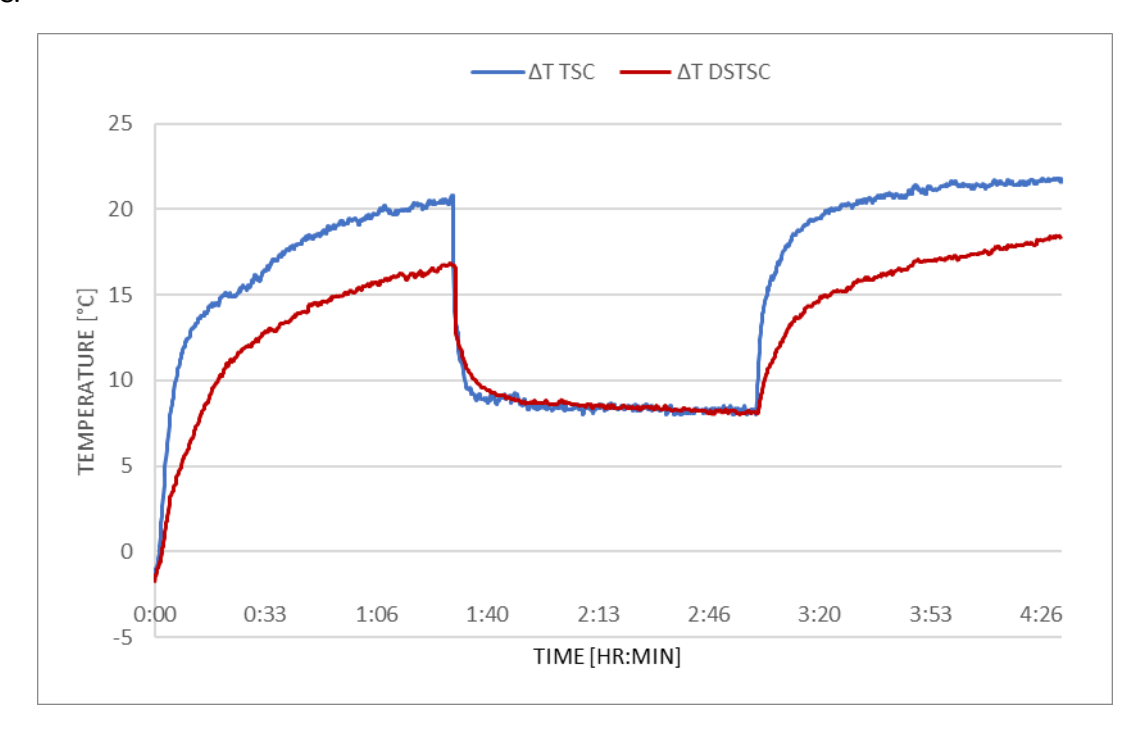


Figure 25. Temperature difference between ambient and outlet air

Figure 26 zoom right after starting the fan, we can observe that during a short time of about 15min, the DSTSC produced more energy than the TSC. This can be due to the second absorbent plate placed at the back of the perforated absorber plate which releases the energy stored, in the case of a strong



flow, of 500m3 / h, the temperature difference stabilizes around of the same value, approximately 8.4° C, 25 minutes after starting the fan.

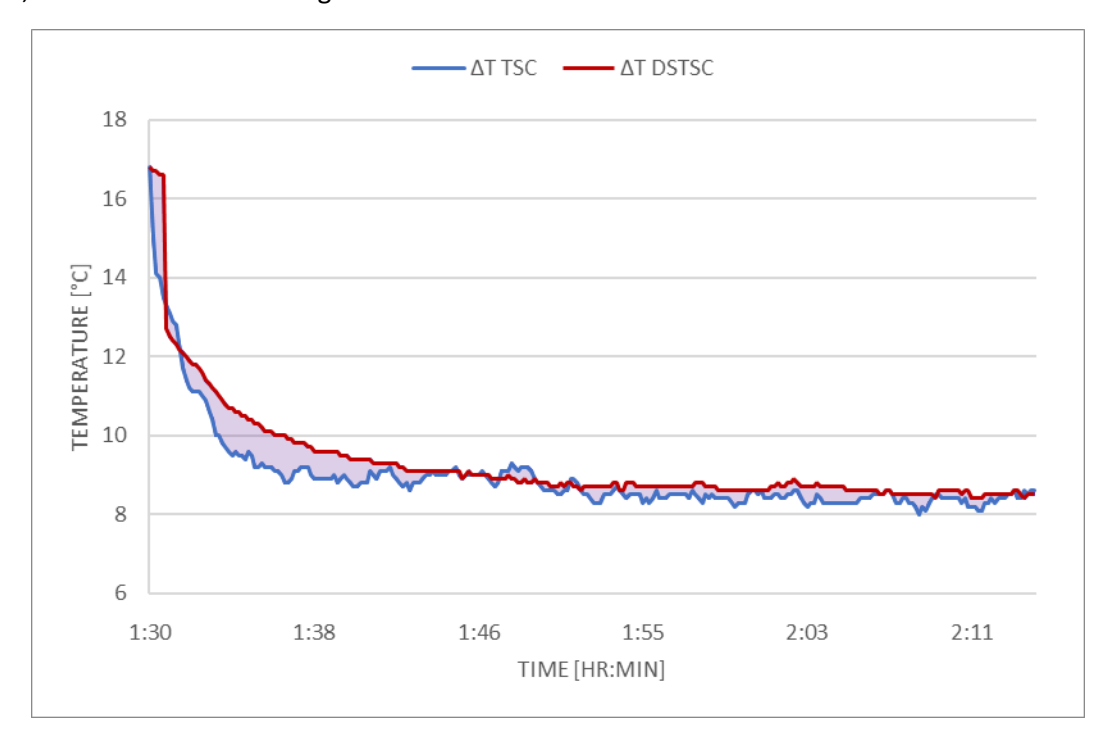


Figure 26. Temperature difference between ambient and outlet air after switching on the fan

We calculated the area under each plotted curve with trapezoidal rule suitable for Excel, then sum up these areas and finally we calculate the difference between the two collectors. Figure 26 shows the area between the two curves representing the difference regarding the energy production of each collector.

$$P = c_{p,air} * m_{air} * (T_{air,out} - T_{amb})$$
⁽¹⁾

$$m_{air} = \frac{Q_{air} * \rho_{air}}{3600} \tag{2}$$

$$E = P * t \tag{3}$$

Where $T_{air,out}$ the outlet air temperature (K), T_{amb} the outside ambient temperature (K), T_p the average temperature of the absorber plate (K), $C_{p,air}$ specific heat capacity of air (J/kg.K), m_{air} mass flow rate of air through the collector (kg/s), Q_{air} air flow rate [m³/h], ρ_{air} air density [kg/m³, E energy production [kWh], P power or heat capacity [kW].

Table 6 shows the total energy produced by each collector during 45min, from 1:30 to 2:15 based on the above expressions to calculate the power and energy. The Double Skin Transpired Solar Collector produced only 41.6Wh more than the TSC. We can then conclude that there is no major difference between the two collectors, especially if we consider the accuracy of thermocouples of ± 1.3 °C.

Table 6. From 1:30 to 2:15

TCC DCTCC Diff			
130 03130 0111	TSC	DSTSC	Diff



P _{average} [kW]	1.503	1.558	0.055
E [kWh]	1.123	1.164	0.041
E [Wh]	1123	1164	41

2.2.2. Intermittent solar radiation

Methodology for intermittent solar radiation:

We first turn on the solar simulator for 25min until the plate reach the stagnation point where the temperature no longer increases. Then we simulate an intermittent solar radiation by turning on and off the solar simulator for different periods of time:

- 25min solar simulator On and fan Off
- 20min solar simulator On and fan On
- 10min solar simulator Off and fan On
- 10min solar simulator On and fan On
- 20min solar simulator Off and fan On
- 20min solar simulator On and fan On
- 5min solar simulator Off and fan On
- 5min solar simulator On and fan On

Figure 27 and Figure 28 show the temperature difference between ambient and outlet air for TSC and DSTSC at $400 \, \text{m}^3 / \text{h}$ and $500 \, \text{m}^3 / \text{h}$.

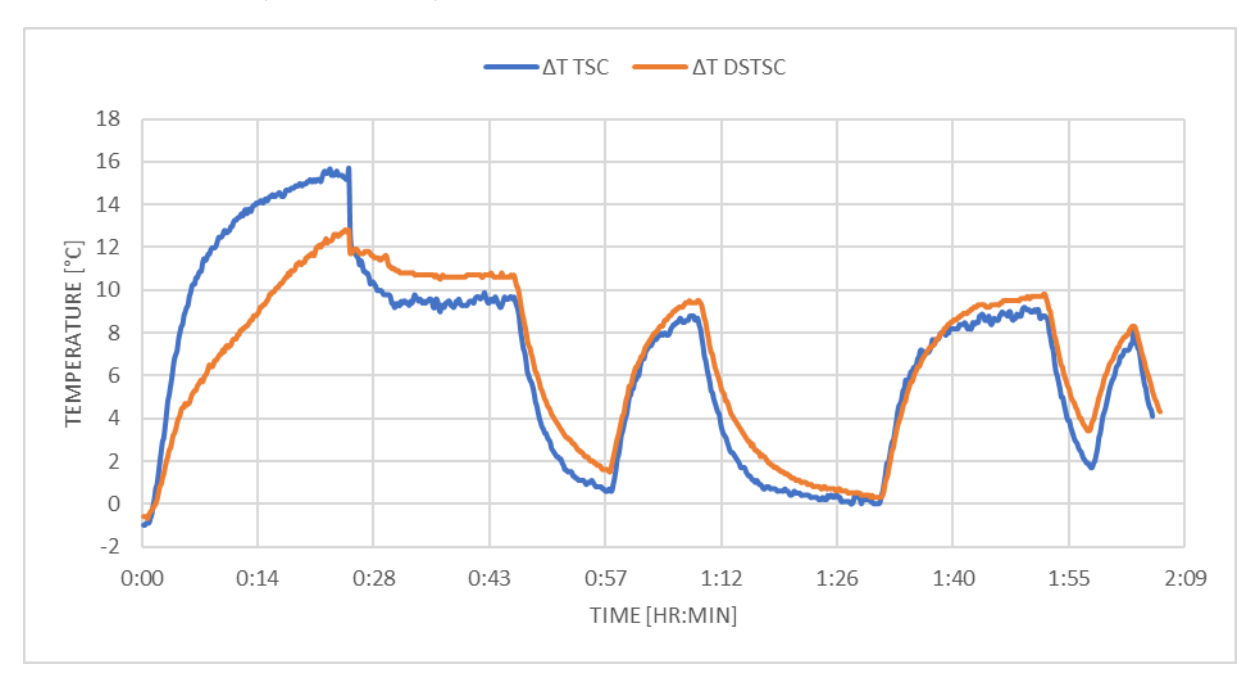


Figure 27. Temperature difference between ambient and outlet air for TSC and DSTSC at 400m³/h.



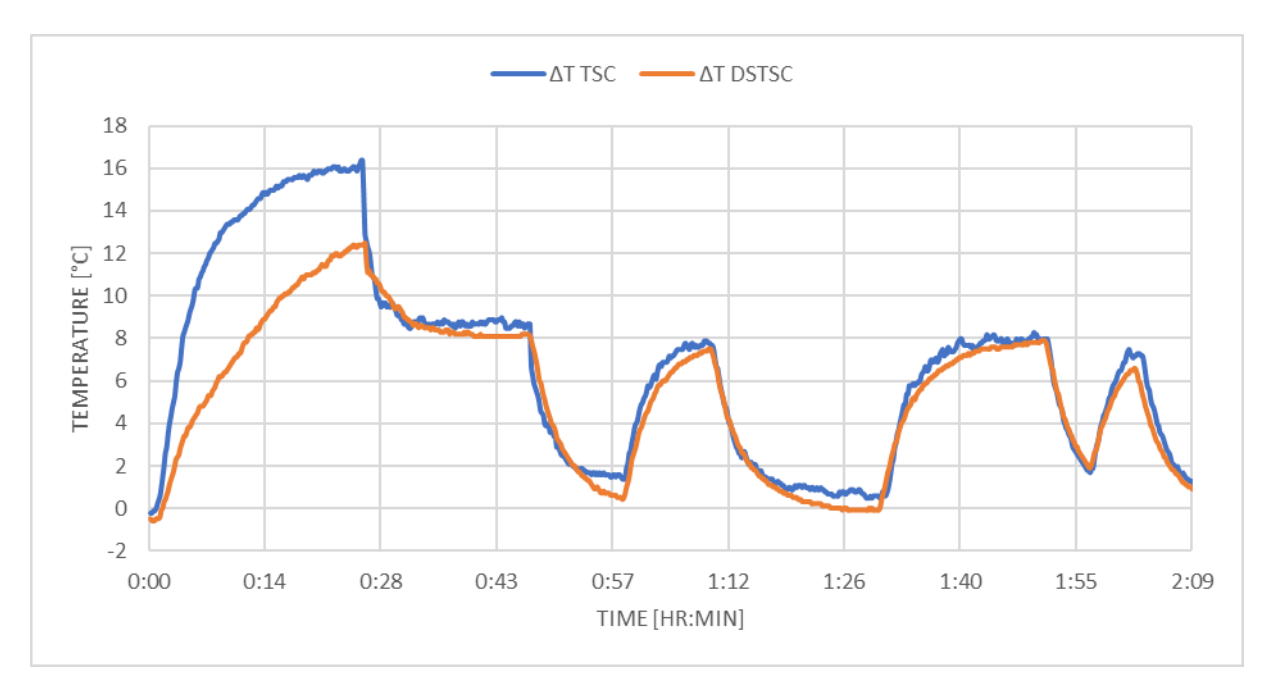


Figure 28. Temperature difference between ambient and outlet air for TSC and DSTSC at 500m³/h.

Table 7 and Table 8 compare the heat capacity and energy produced by each collector at 400m³/h and 500m³/h.

Table 7. Heat and energy capacity at 400m³/h

	TSC	DSTSC	Diff (DSTSC – TSC)
P [kW]	0.6846	0.8025	0.1179
E [kWh]	1.2780	1.4981	0.2201
E [Wh]	1278	1498	220

Table 8. Heat and energy capacity at 500m³/h

	TSC	DSTSC	Diff (DSTSC – TSC)
P [kW]	0.8377	0.7619	-0.0758
E [kWh]	1.5730	1.4307	-0.1423
E [Wh]	1573	1431	-142

The results demonstrated in this chapter regarding the indoor experimental study match with the CFD results previously obtained, it argued that the DSTSC is more efficient than the TSC until 450-500 m3/h, and after 500 m3/h the DSTSC becomes less efficient. It is important to note, that the present evidence relies on a by-pass on the upper part of the collector, as we mentioned during the numerical study.

One limitation of this first experimental study is that it is not including the outdoor climatic conditions that can influence the thermal performance of the solar air collectors. Thus, a second experimental study in outdoor condition was conducted and we present it in the next chapter.



3. Outdoor experimental studies

3.1. Material and methods

3.1.1. Measuring devices

3.1.1.1. Outdoor solar radiation

We have experimentally determined the part of diffuse and direct radiation composing the global solar radiation measured using the Ahlborn "Star Pyranometer Type FLA628S" pyranometer.

For this we took an opaque plate used as a solar mask to stop direct solar radiation on the pyranometer and thus allow only diffuse solar radiation to pass.

Table 9. Solar radiation composition

Radiation Solaire globale	Radiation Solaire Diffuse	Radiation solaire directe
501,5 W/m ²	112,1 W/m²	389,4 W/m²
100%	22,4%	77,6%

Table 9 help us to have a better appreciation of the composition of the global solar radiation measured by the FLA628S pyranometer, so only 22.4% of the global solar radiation is composed of diffuse radiation. This allows us subsequently to correctly enter the values of solar radiation as a function of the diffuse and direct components in computational fluid mechanics software.

3.1.1.2. Wind velocity

In this part we present the instrumentations for wind velocity and wind direction. We placed on a rooftop near the Solar Façade a wind direction sensor, Type FVA614, and a wind velocity sensor, Type FVA615-2 (Figure 29), for measuring the horizontal wind direction and velocity.

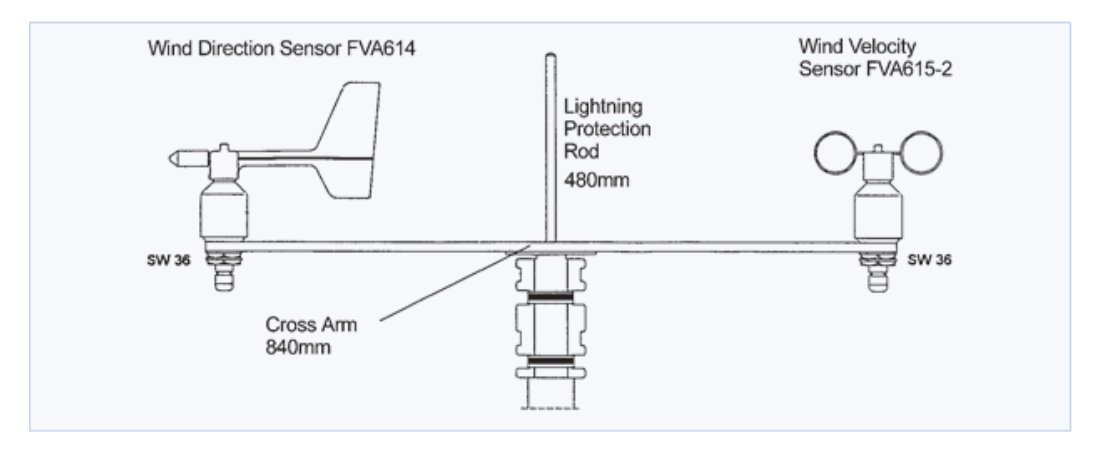


Figure 29. Scheme of the device for wind velocity and wind direction



Table 10 and Table 11 presents the specifications of the wind direction sensor, Type FVA614, and a wind velocity sensor, Type FVA615-2.

Table 10. Technical data for Wind Velocity Sensor Type FVA615-2

Measuring range	0.5 to 50m/s	
Accuracy	±0.5m/s ±3% of meas. value	
Resolution	0.1m/s	
Operative range	-30 to +70 °C, with heating	

Table 11. Technical data, Wind Direction Sensor Type FVA614

Measuring range	00 to 360°	
Accuracy	±5°	
Resolution 11.25° (5 bit Gray code)		
Operative range	-30 to +70 °C, with heating	

3.1.2. Outdoor solar facades

In total three solar air collectors have been integrated in façades. One TSC and DSTSC integrated on the façade of the laboratory building (Figure 33), and one DSTSC integrated in a container. The two collectors integrated in the laboratory façades are used to characterize the thermal behavior of both collectors in outdoor conditions. And the DSTSC integrated in the container façade is combined with a drying chamber and used for solar drying process. Figure 30 shows the container before and after the integration of solar air collectors. SAC have been integrated in place of doors. This implantation shows the ease of use of this type of building integrated solar air heater. On the left of the picture, we observe the DSTSC used for drying needs and on the right a prototype of glazed transpired solar collector used by our team for another experimental study.







Figure 30. Container with integrated Solar Air Collectors

Fans have been alimented with two high precisions power supplies ZHAOXIN design for laboratory. Output voltage and current are adjustable. Table 12 shows the specifications of the power supply units.

TOURS OF MANAGEMENT BLAND

SERVICE STATES OF THE STATES OF

Table 12. Power supply unit specifications

Zhaoxin RXN.PS.JPS		
Input voltage	AC 110V/220V	
Voltage stability	≤0.01%+2mV	
Load stability	≤0.01%+2mV	
Recovery time	≤100µS	

Airflows have been determined using the FlowFinder mk2 presented in the paragraph 2.1.2.2.

3.1.3. Solar dryer

Figure 31 shows the 3D geometry of the drying chamber designed with SolidWorks 2020 besides the real scale drying chamber under construction. The drying chamber consist into a box made of wood, insulated with rockwool, and covered in the inside with aluminum for hygienic reasons. Indeed, wood-based materials emits various organic chemical substances, mostly volatile organic compounds (VOCs) such as limonene or formaldehyde have possible health effects. We made the choice to use principally wood materials the less metal-based materials for more sustainability in the concept, however we did not neglect the hygienic and health priority. The wood box is connected to two cones made of aluminum pre-insulated used for HVAC Air Ducts (ALP). These materials are easy-to-use and manufactured, and they combine two important factors for us, they are hygienic and insulated so we don't need to add insulation materials such as rockwool. Cones have been used with regards to the airflow, as studied in the second research report with CFD simulations. At last, 3 drying trays made of wood frames and stainless-steel mesh have been placed in the drying chamber.



The drying chamber will be then connected to the Double Skin Transpired Solar Air Collector.

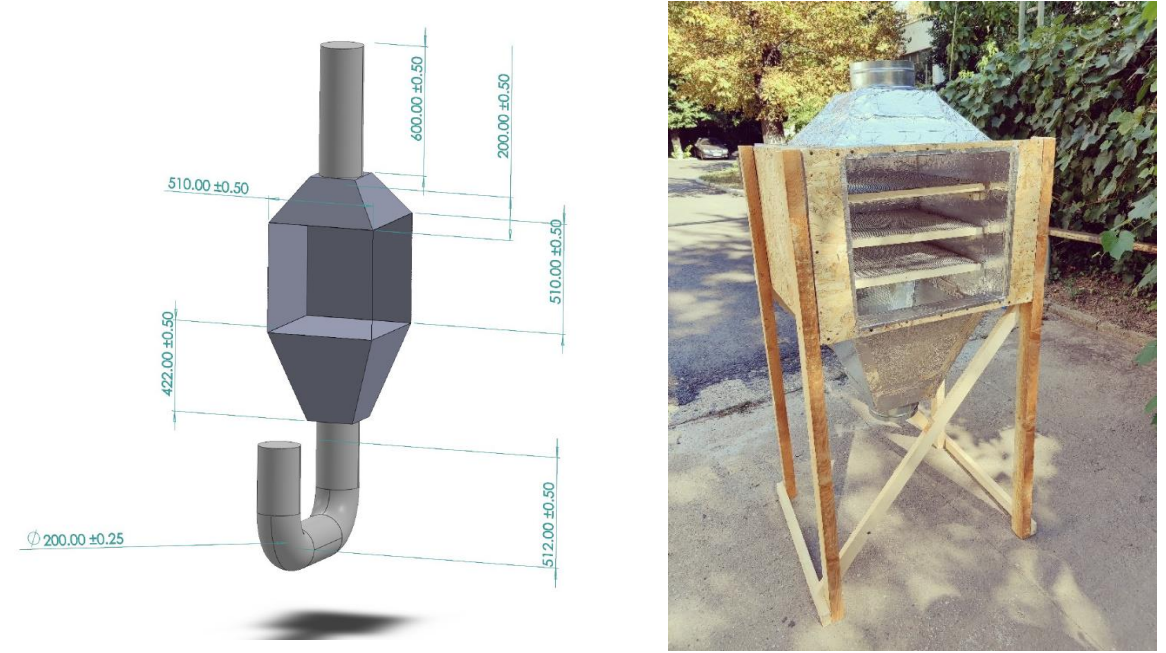


Figure 31. Drying chamber

3.1.4. Governing equations

The heat exchange effectiveness can be calculated with the following expression:

$$\varepsilon_{HX} = \frac{T_{outlet} - T_{ambient}}{T_{Absorber\ plate} - T_{ambient}} \tag{4}$$

where: T_{outlet} is the outlet air temperature [°C]; $T_{ambient}$ is the ambient air temperature [°C]; $T_{absorber}$ plate is the temperature of absorber plate[°C].

Solar collector's efficiency can be calculated with the following equation:

$$\eta = \frac{c_{p,air} \, m_{air} \left(T_{air,out} - T_{amb} \right)}{I_T \, A_S} \tag{5}$$

With $T_{air,out}$ the outlet air temperature (K), $T_{air,out}$ the outside ambient temperature (K), T_{p} the average temperature of the absorber plate (K), $C_{p,air}$ specific heat capacity of air (J/kg.K), m_{air} mass flow rate of air through the collector (kg/s), I_{T} incident solar radiation on the collector (W/m²) and A_{S} surface of the solar collector (m²).

Another expression have been proposed by Van Decker et al. [16] if the efficiency of the heat exchanger is known:

$$\eta = \frac{\alpha_s}{1 + \frac{h_r}{\varepsilon_{HX} \rho_{air} c_{p,air} v_s}} \tag{6}$$



With α_s the absorption coefficient of the perforated plate, h_r the radiation exchange coefficient (W / m^2 .K), pair the air density (kg / m^3) and v_s the air outlet speed (m / s).

The term h_r comes, according to the law of Stéphan Boltzmann, from the formula of the heat flow exchanged between a surface S and an ambient medium:

$$\Phi(W) = \varepsilon . \sigma . S . (T_S^4 - T_a^4) \tag{7}$$

With σ the Stefan Boltzmann constant, 5.67.10⁻⁸ W.m⁻².K⁻⁴, S heat exchange surface (m²), ε emissivity of the collector surface, T_S temperature of the black body (K) et T_a ambient temperature (K).

The expression of the heat flow being nonlinear because it involves temperatures at the fourth power, it is necessary to linearize the expression which is acceptable when the temperature difference $T_S - T_a$ remains low. The relation then becomes after linearization:

$$\Phi(W) = h_r . S. (T_S - T_a) \tag{8}$$

where,
$$h_r = 4 \cdot \varepsilon \cdot \sigma \cdot T_m^3$$
 (9)

 T_m the mean temperature between T_S et T_a .

La formulation de Van Decker pour exprimer l'efficacité d'un collecteur solaire est donc reposé sur le fait que la température de la plaque perforée soit proche de de la température ambiante ce qui est à priori pas corrects dans la plupart des cas. Les valeurs de ces rendements présentés seront donc à prendre avec des pincettes.

pair density of air (kg/m³) can be calculated using the following formula:

$$\rho_{air} = \frac{p}{R_{specific} * T} \tag{10}$$

Where, $R_{specific}$ = R/M_d, R is the universal constant of ideal gases and M_d the molar mass of air. The universal ideal gas constant is the product of the Avogadro number N_A and Boltzmann's constant k_B, 8,314 462 618 153 24 J mol⁻¹ K⁻¹. Considering that the molar composition of air varies very little, then R= 287.058 J/(kg·K). p (Pa) is the absolute pressure - atmospheric pressure being 101 325 Pa- and T (K) absolute temperature.

3.2. Control strategies

The main idea of the prototype of Building Integrate Solar Dryer presented in Figure 32 is to use the PCM storage only when there is a need, a system of thermal management of the storage based on dampers. Please find attached a scheme of the system. Here is how the system works:

- Mode 1: Charge
 - o Damper 1 close
 - o Damper 2 open
- **Mode 2**: By-pass (when by-passing we reduce the pressure drop, and thus reduce the fan consumption)
 - o Damper 1 open



- Damper 2 close
- Mode 3: Discharge
 - o Damper 1 close
 - o Damper 2 open

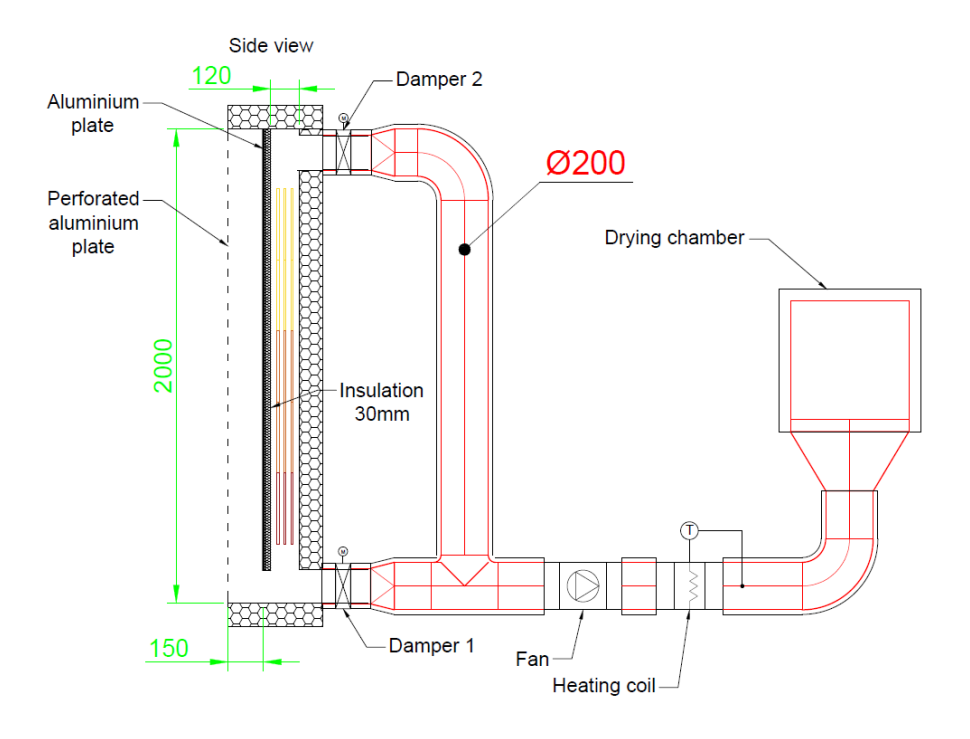


Figure 32. Building integrated solar dryer

The construction of drying chamber is based on the concept optimized during computational fluid dynamics studied in the Research Report 2 "Optimization of transpired solar collectors for drying needs via computational fluid dynamics".

Saini et al. have defined flow control strategy [20] for an UTSC integrated into an Exhaust air heat pumps (EAHP). In this configuration the UTSC is used to pre-heat the air for the HP evaporator added to recycled exhausted air of the building. Two strategies have been defined, one with variable air flow and another with constant air flow in the UTSC, Figure 32Error! Reference source not found. presents the global strategy of the system.

The fan of the TSC is controlled in function of the outlet temperature of the collector and the solar irradiation. First the fan turns on when the solar irradiation is greater than 50 W/m². Then the air mass flow rate (m), presented in the equation (11, is calculated in function of the collector outlet air temperature and the exhaust air of the building ventilation (T_{exh}).

$$m = \frac{G_{t} \cdot \eta}{C_{p} \cdot (T_{exh} - T_{amb})}$$
(11)

Where: η is the efficiency of the TSC, G_t is global irradiation, Cp is the specific heat capacity of air and T_{amb} is the ambient air temperature.

3.3. Results & Discussions



3.3.1. Solar Façade lifetime issues

The first issue that we encountered with our solar facade is regarding the behavior of the coating. The black electrostatic coating used by our supplier was not the best coating for exterior usage. Figure 33 shows the two solar façades, the one on the left stayed approximatively 2 years in outside conditions and the one on the right is new. We can notice that the coating is not resistant and cannot be recommended for solar facades usages. This issue revelated the importance of the materials used for solar collector construction for long time utilization. Regarding this topic we can think further than a resistant coating for exterior conditions, for future works intelligent coating could be used such as air purifying and photocatalytic paints [21, 22] to transform the perforated metal absorber into an air purifier system.



Figure 33. Solar façade after 2 years (left), new solar façade (right).

3.3.2. Thermal behaviours

The main focus of the experiments was to analyze the thermal behavior, to determine the heating and energy production capacity of TSC and DSTSC during summer conditions for drying needs.

Table 13. Minimum and maximum airflow values.

Air flow	TSC	DSTSC
Min [m³/h]	447	443
Max [m³/h]	451	450

For the outdoor experiments the two fans have been set at ±450m³/h. The two power supply units are not providing perfectly constant current there is a fluctuation in the output voltage and current intensity, Table 13 shows the airflow range for both solar collectors.



Figure 34 shows the variation of solar radiation and the temperature of TSC, DSTSC and ambient air for 3 days of monitoring. The effect of solar radiation on collector's outlet temperature is easily visible.

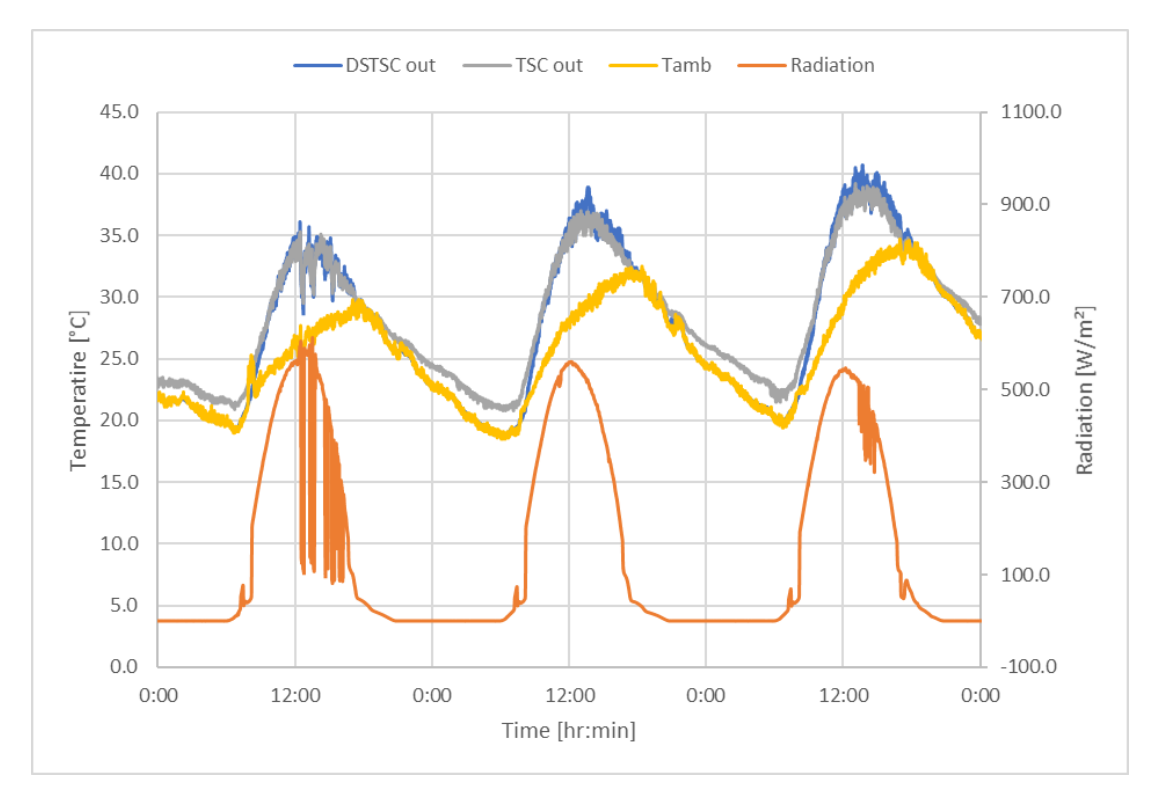


Figure 34. Variation of solar radiation and the temperature of TSC, DSTSC and ambient air.

One concern about the findings of the experiments is regarding the calibration of the thermocouple used to monitor the outlet temperature of the TSC. Indeed, we can observe in each figure that even during night when there is no solar radiation, the TSC still has a higher temperature than the ambient air. It is to mention that thermocouples have an accuracy of ±1.3°C. It is notable that in a certain range of temperature, between 20°C and 25°C the thermocouple at the TSC outlet is no longer accurate, the divergence reaches a maximum of 2 degrees, it is higher than the accepted range of accuracy. Thus, for future measurements this thermocouple should be calibrated.

Figure 35 presents the temperature difference (ΔT) of TSC and DSTSC in function of the time during 3 days of monitoring. During these three days we had a variation of the ΔT between 0°C and approximatively 10°C for both solar collectors for an airflow of 450m³/h.



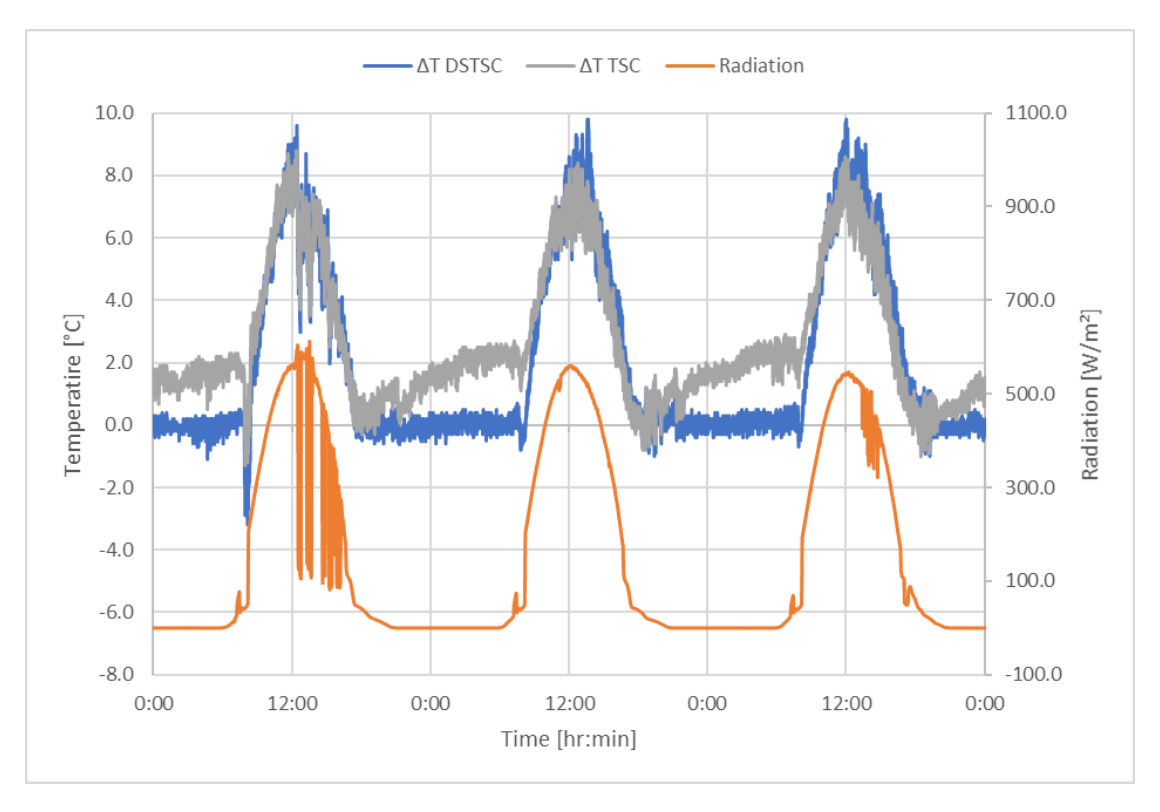


Figure 35. Variation of solar radiation and the temperature difference (ΔT) of TSC and DSTSC.

Figure 36 and Figure 37 closely look to the variation of the temperature difference (ΔT) of TSC and DSTSC for an intermittent solar radiation day. It is notable that both solar collectors have a low thermal inertia, the response time of the outlet temperature at each variation of the solar radiation is very fast.

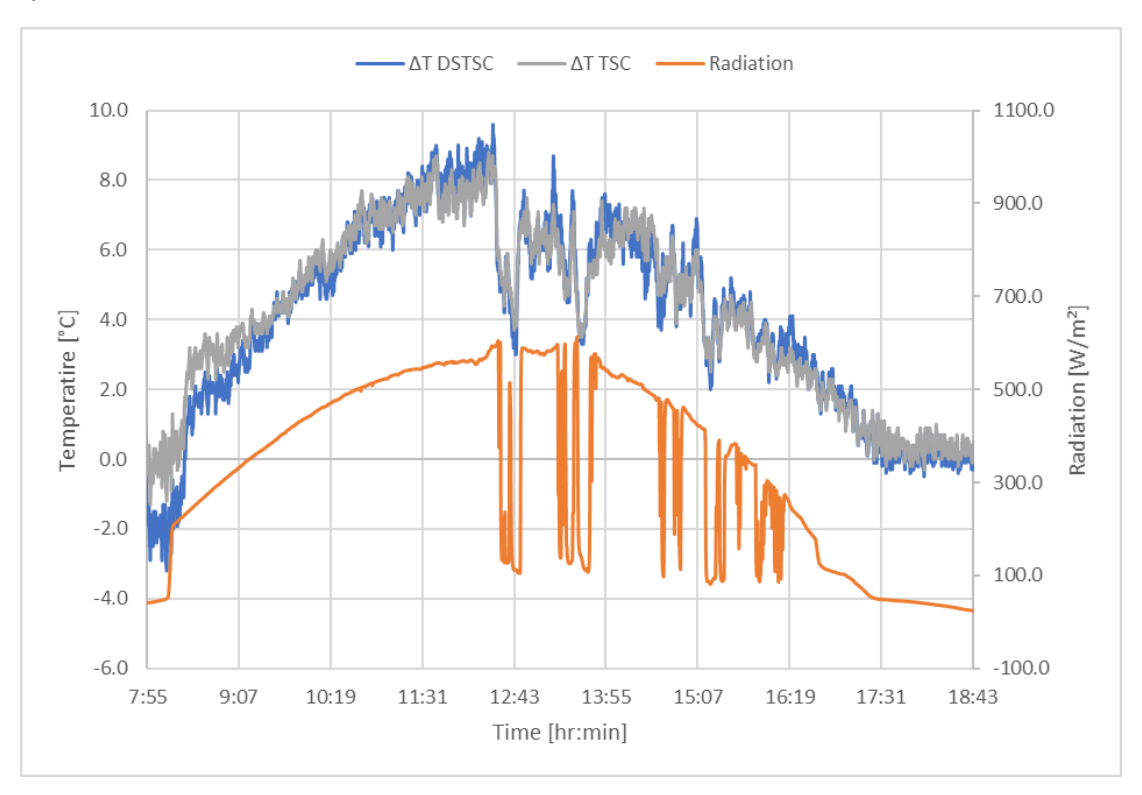


Figure 36. Variation of the temperature difference (ΔT) of TSC and DSTSC for an intermittent solar radiation day.



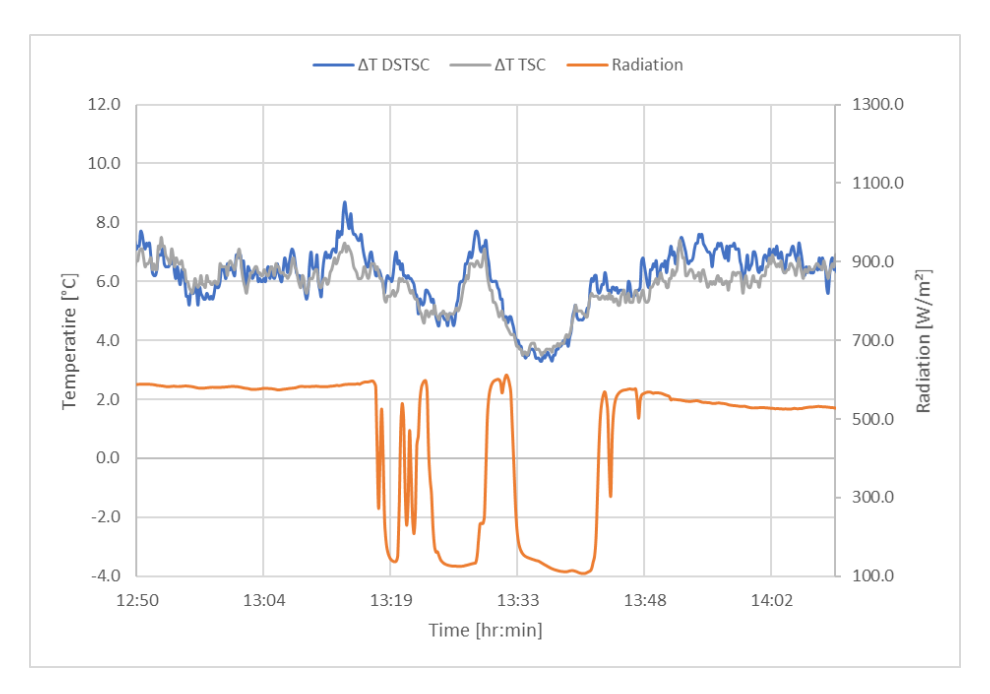


Figure 37. Zoom on the variation of the temperature difference (ΔT) of TSC and DSTSC for an intermittent solar radiation day

The observations made during the numerical studies regarding the thermal behavior and differences between the two solar facades for intermittent solar radiation cases are no longer obvious. On the contrary, the two collectors have very similar behaviors.

3.3.3. Heating and energy production capacity

This part of the data analysis focus on the characteristics of the TSC and DSTSC. Useful characteristics for building system designer have been calculated, such as the heating capacity and the energy production.

Figure 38 depict the variation of the heating capacity for three different days. The heating capacity varied from 0kW during nighttime to 1.5kW for a solar radiation of 560 W/m².



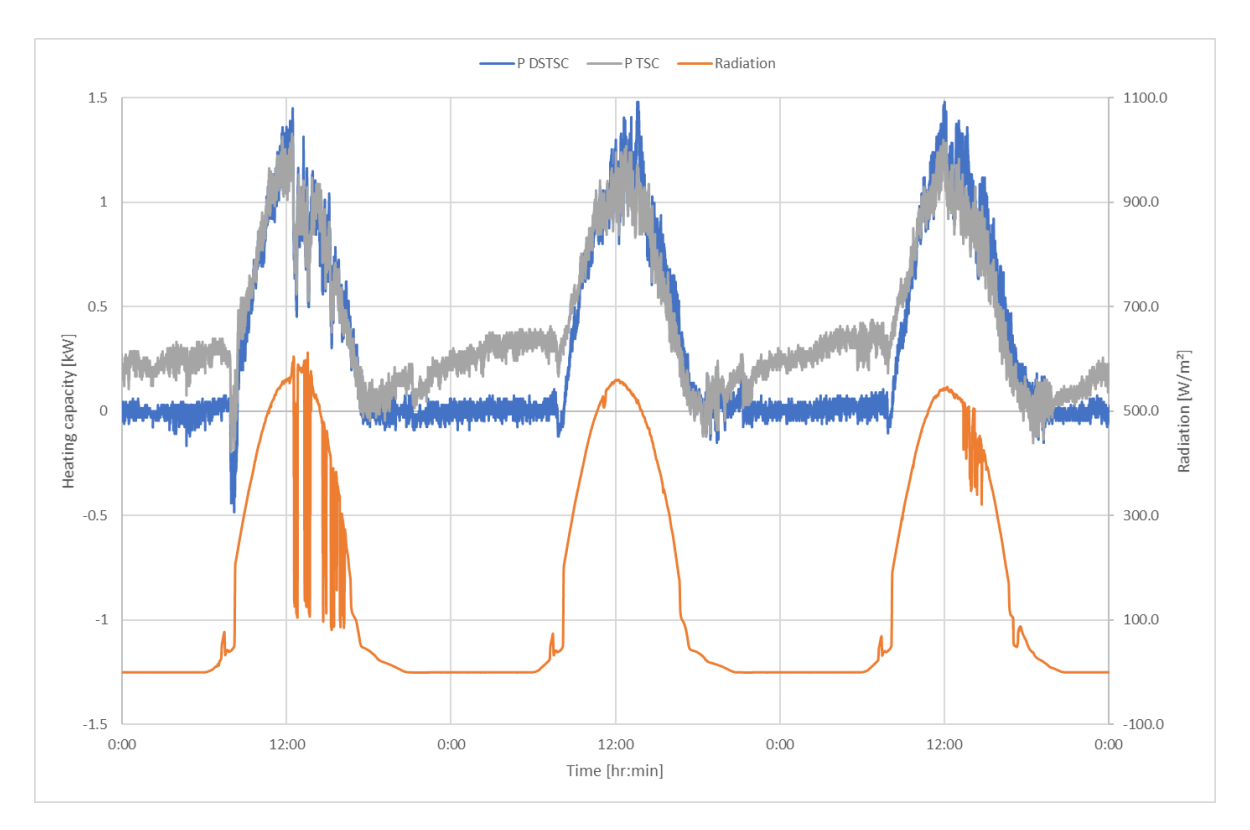


Figure 38. Variation of the heating capacity and solar radiation.

To investigate this statistically, we calculated the average heating capacity of both solar collectors and the energy production for a constant solar radiation day, for a 8 hours usage, between 9am and 5pm. Table 14 presents the data. Our data show that there is a very small difference regarding the heating capacity of the two collectors.

	DSTSC	TSC	Diff (DSTSC – TSC)
P _{average} [kW]	0.8113	0.8050	0.0062
E [kWh]	6.490	6.440	0.0497
E [Wh]	6490	6440	50

Table 14. From 09:00 to 17:00

Figure 39 and Figure 40 show the variation of the solar collectors' efficiencies and absorber plates' effectiveness from 09:00 to 17:00 during the same day as the value from the Table 14 have been calculated. Absorber plates' effectiveness have been calculated with the equation (4) considering the average temperature of the absorber plate. The average temperature of the absorber plate have been determined with at least 3 thermocouples in three different zones.



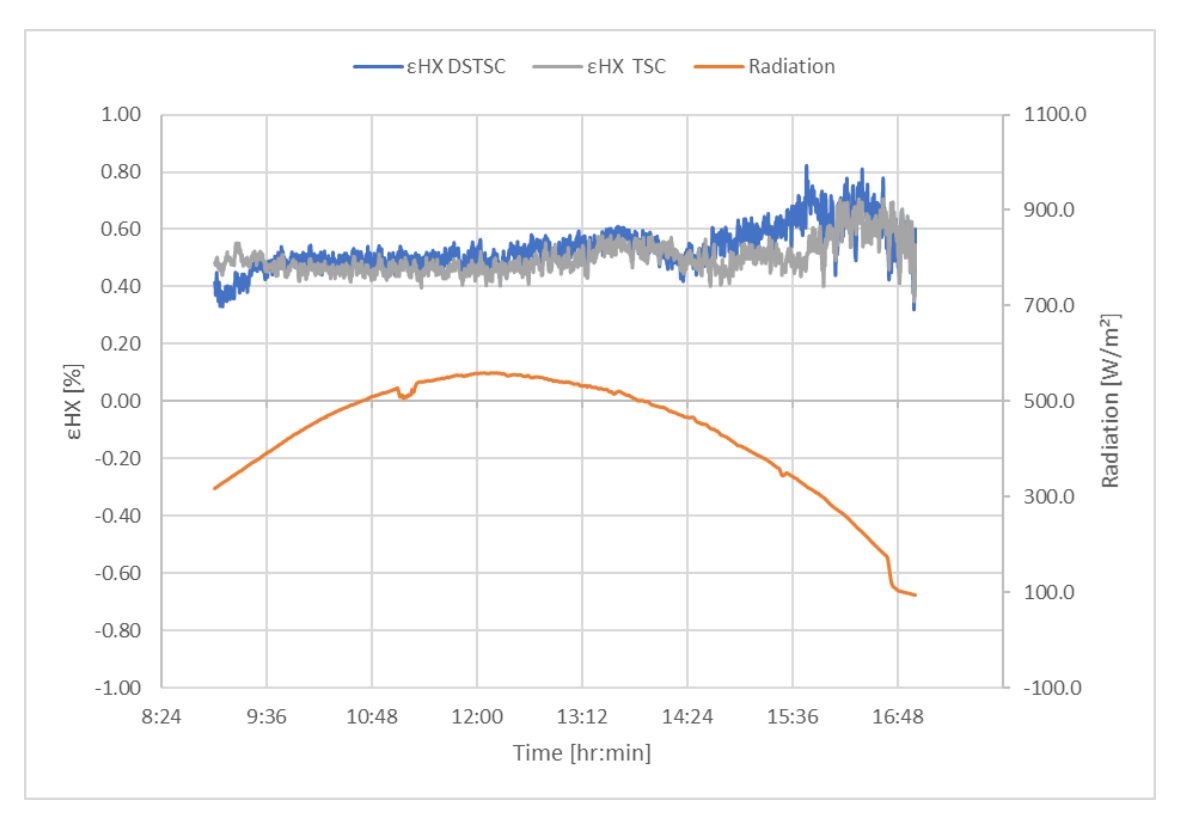


Figure 39. Variation of the absorber plates' effectiveness and solar radiation from 09:00 to 17:00.

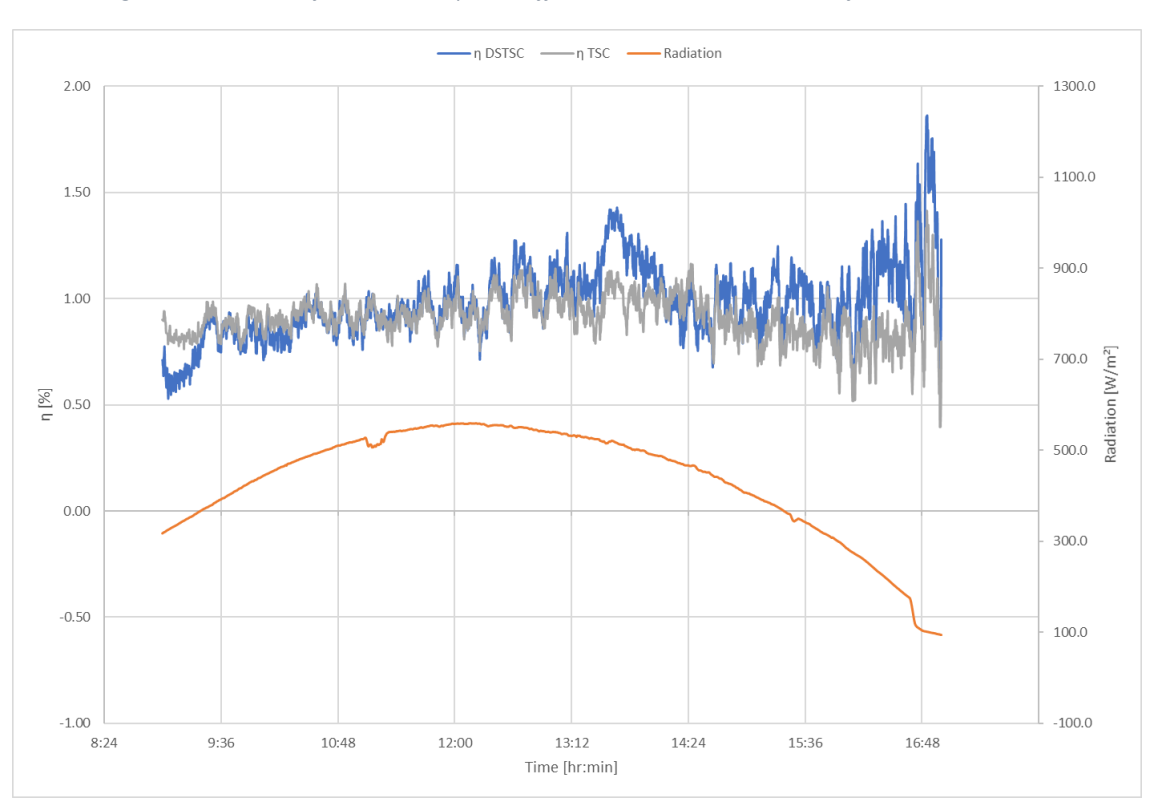


Figure 40. Variation of the solar collectors' efficiencies and solar radiation from 09:00 to 17:00.

We can observe that even if solar radiation is stable the solar collector efficiency is still variable. We speculate that this might be due to the wind. Thus, we investigated the effect of the wind velocity on the solar collector efficiencies, Figure 41 & Figure 42.



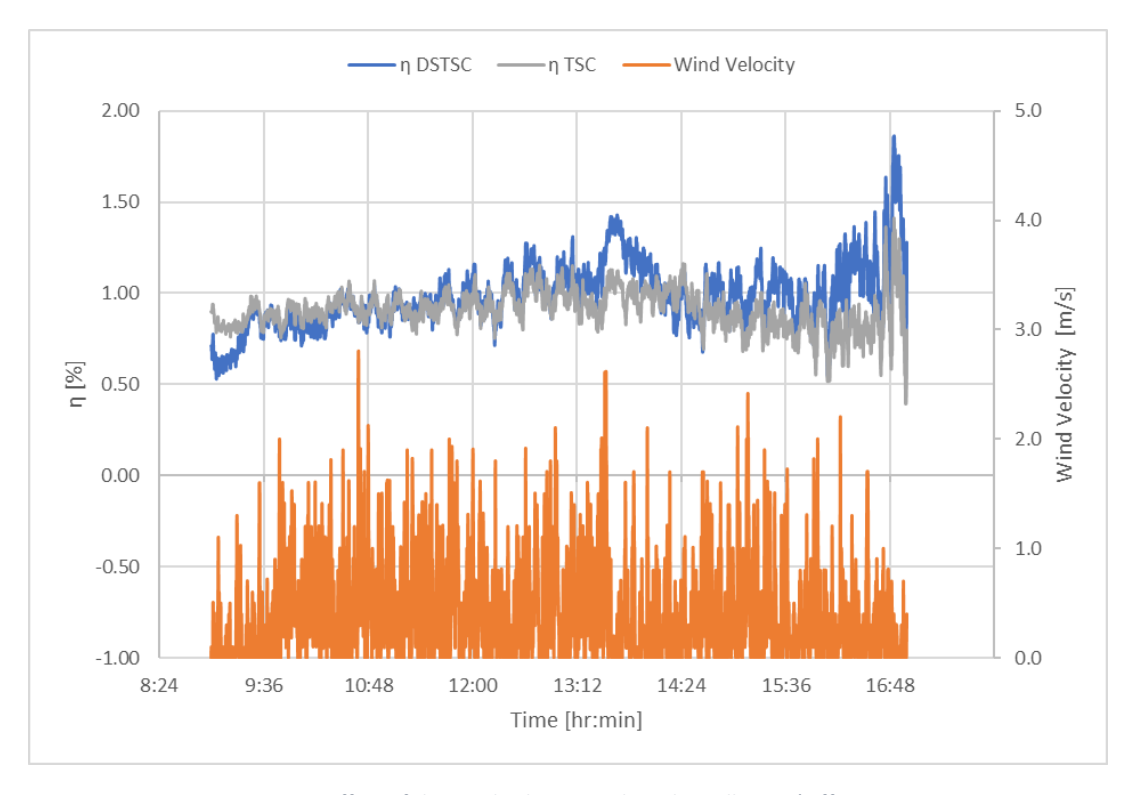


Figure 41. Effect of the wind velocity on the solar collectors' efficiencies

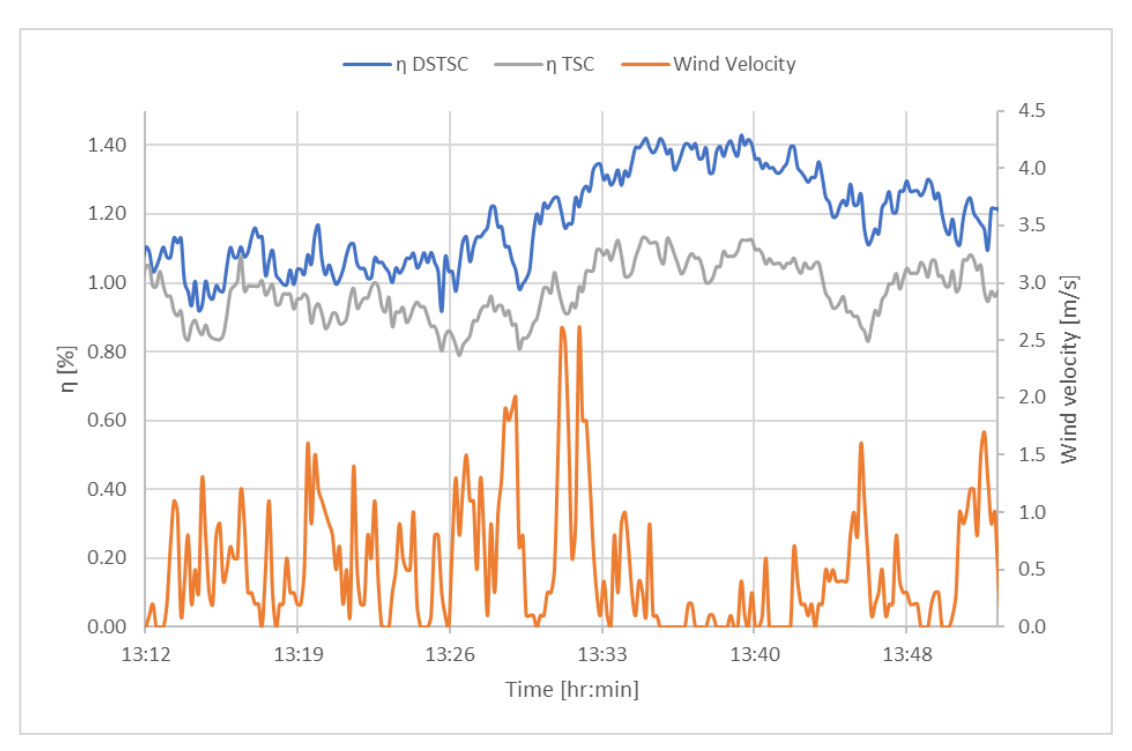


Figure 42. Zoom on the effect of the wind velocity on the solar collectors' efficiencies

It remains unclear to which degree the small variation of the solar collector efficiency and absorber effectiveness are attributed to the wind velocity. This is desirable for future work to investigate the effect of the wind for high wind velocity magnitude.



3.3.4. Simplified method for evaluating thermal performance TSC and DSTSC

This method uses the chart trendline to get an equation for the plotted curves of each collector. Figure 43 shows the two curves representing the evolution of the temperature difference between the inlet and outlet air of the TSC and DSTSC in function of the solar radiation for an air flow of 450m³/h. We introduced two second order polynomial trendlines to evaluate the thermal performance of both solar collectors.

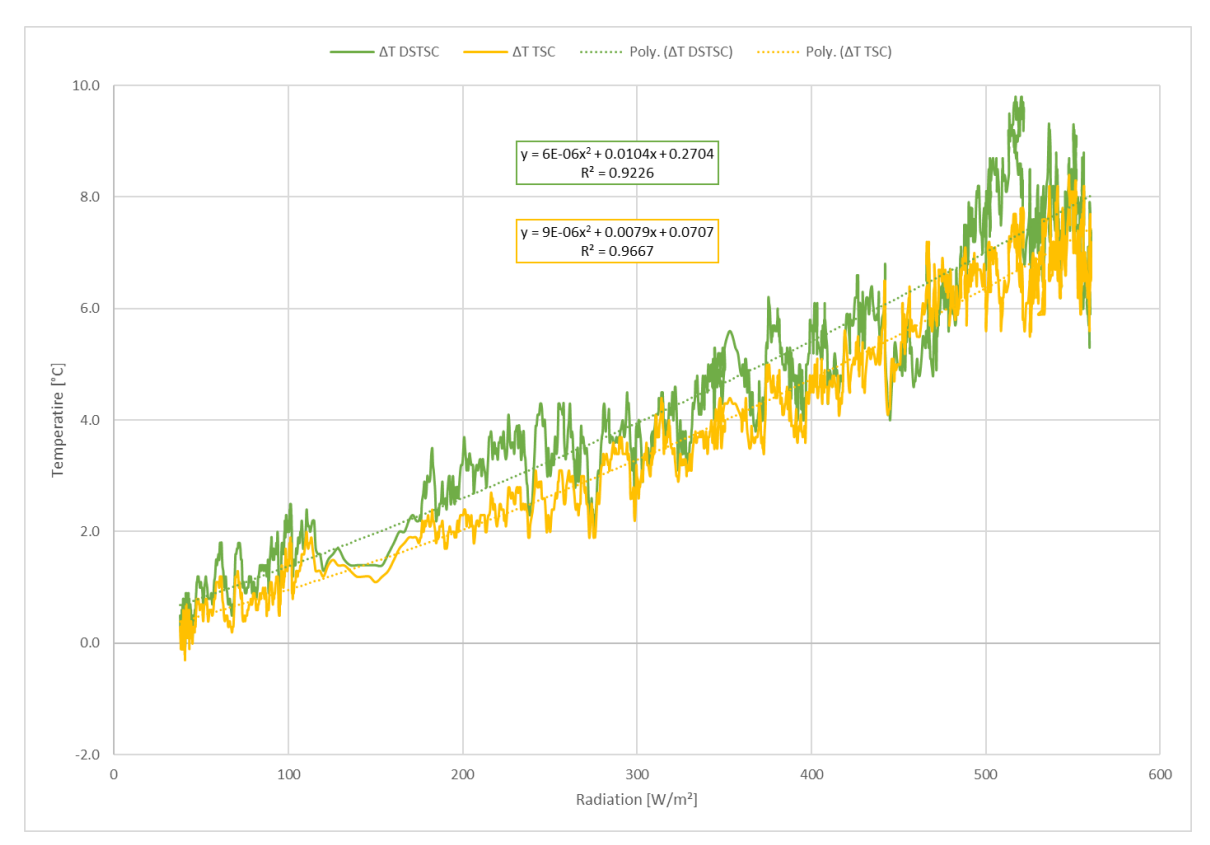


Figure 43. Evolution of the ΔT in function of the solar radiation at 450m³/h.

Equation (12 shows the second order polynomial to evaluate the thermal performance TSC:

$$y = 9E - 06x^2 + 0.0079x + 0.0707 (12)$$

Equation (13) shows the second order polynomial to evaluate the thermal performance DSTSC:

$$y = 6E - 06x^2 + 0.0104x + 0.2704 (13)$$

For the moment these equations only help us to determine the thermal performance of TSCs in function of solar radiation. Another challenge is now to evaluate the thermal performance of solar collectors for multicriterial climatic conditions, such as the influence of the wind speed previously mentioned. Even if results have revealed a small influence of the wind on the thermal performance of solar collectors at least for summer conditions when the wind speed is within a range of 0 to 5m/s. Future investigations, for autumn or winter condition - when wind velocity magnitude is higher - are necessary to validate the conclusion that can be drawn from this study.



4. Conclusion and future works

These preliminary experimental studies give us consistent feedback regarding the thermal behavior of TSC and DSTSC for both indoor and outdoor conditions. Results confirmed that for our range of airflow 300-500m³/h., there is no major differences between the two collectors, thus the use of DSTSC for our future works on building integrated solar dryers. The main objective of the DSTSC is to create a space to integrate a thermal energy storage without affecting the thermal performance of basic Transpired Solar Collectors. In our future works we will integrate a TES based on PCM in the back-pass of the DSTSC. Different PCM arrangement and encapsulation shapes will be investigated. Figure 44 depict the scheme of the experimental stand that will be used for the investigation of Thermal Energy Storage integrated in the DSTSC. The stand consists into a plexiglass air duct connected to a heating coil and a fan. Different PCM shape will be investigated, such as spherical and rectangular encapsulation. Additionally, the effect of cascaded PCM will be investigated. In the literature, cascaded PCMs have improved the thermal performance of the latent heat storage systems, more uniform melting/solidification, increased energy and exergy performance, more efficient charging and discharging phase. Liu, Iten and Shukla [23] conducted a numerical study to assess the potential of cascaded PCMs for free cooling applications in buildings. PCMs with different melting temperature have been investigated to find an optimal combination. Results have shown that the best combination is for RT20 with RT25 with an average effectiveness of 0.5.

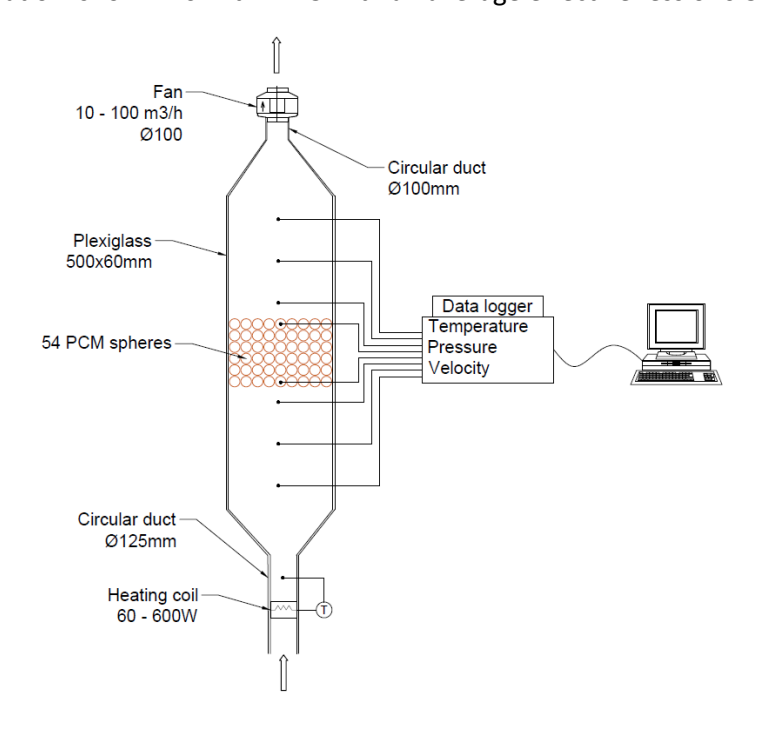


Figure 44. Experimental stand for TES investigations

Our future research will also consider the potential effects of integrated metallic mesh to increase the thermal response of the TES. Macro and nano enhanced PCM have been widely adopted in the field of Thermal Energy Storages for buildings and renewable energies [24, 25]. Li [26] analyzed via CFD simulations the heat transfer inside a ventilation system for building heating based on paraffin RT30 integrated in sinusoidal encapsulations. Alumina (Al_2O_3) nano-sized material were added in the paraffin with fraction of 0.04 to enhance the conductivity of the latent heat storage. The most time-efficient configuration belongs to the cases with alumina nano-powders, results have shown a decrease in solidification time of 5.49%. Combining Al_2O_3 nanoparticle with metallic fins in PCM



storages [27, 28] have shown even better results, indeed, solidification and melting time can be reduces by 12 and 6.4%, respectively. The integration of nano carbon and nano coconut shell have been investigated by Sun, Liu et al. [29]. Oleic acid and span 80 have been used to mitigate the agglomeration of nanoparticles during melting phases. The optimal concentration of nanoparticles was 0.02 wt% and combined with oleic acid a shorter melting time with 21% was reached compared to pure paraffin. Despite a more sustainable profile the nano coconut shell was less effective than the nano carbon. A challenging problem which arises in this domain is the design of more sustainable PCM and nanoparticles. Xie et al. [30] fixed one of these two issues using an organic PCM nevertheless they still used expanded graphite to improve the thermal characteristic of the thermal energy storage. A new approach is therefore needed for to develop more sustainable thermal energy storage.

5. Dissemination

5.1. Author

October 2021

CIEM 2021

• Article: Investigation of the air layer thickness influence for a novel double skin transpired solar collector

April 2021

Insights of academic youth on the progress of society

- •Info: International student scientific-practical conference EU-Conexus
- Presentation: Think buildings as ecosystems: A case study of a building integrated solar system for urban regeneration

Nov. 2020

Doctoral School Conference 2020

• Prsentation: Mesh independency study for an unglazed transpired solar collector.

Oct. 2020

Enviro 2020

- Article: Mesh independency study for an unglazed transpired solar collector.
- •DOI: http://dx.doi.org/10.1088/1755-1315/664/1/012059

5.2. Co-author

October 2021

CIEM 2021

- Article 1: Mathematical Modelling of Unglazed Transpired Solar Collectors.
- Article 2: Numerical analysis of PCM packed bed heat storage coupled with transpired solar collector.

July 2020

Building Services and Energy Efficiency 2020

- Article: Mesh independency study for a solar glazed transpired collector
- •**DOI**: http://dx.doi.org/10.2478/9788395720413-0069



Bibliography

- 1. Magrini, A., et al., From nearly zero energy buildings (NZEB) to positive energy buildings (PEB): The next challenge The most recent European trends with some notes on the energy analysis of a forerunner PEB example. Developments in the Built Environment, 2020. 3: p. 100019.
- 2. Talaei, M., et al., A Review on Interaction of Innovative Building Envelope Technologies and Solar Energy Gain. Energy Procedia, 2017. **141**: p. 24-28.
- 3. Luo, Y., et al., *Active building envelope systems toward renewable and sustainable energy.* Renewable and Sustainable Energy Reviews, 2019. **104**: p. 470-491.
- 4. O'Hegarty, R., O. Kinnane, and S.J. McCormack, *Review and analysis of solar thermal facades.* Solar Energy, 2016. **135**: p. 408-422.
- 5. Bock, M., *A building integrated solar thermal collector with active steel skins.* Energy and Buildings, 2019. **201**: p. 134-147.
- 6. Smyth, M., et al., Experimental performance characterisation of a Hybrid Photovoltaic/Solar Thermal Façade module compared to a flat Integrated Collector Storage Solar Water Heater module. Renewable Energy, 2019. **137**: p. 137-143.
- 7. Talaei, M., M. Mahdavinejad, and R. Azari, *Thermal and energy performance of algae bioreactive façades: A review.* Journal of Building Engineering, 2020. **28**: p. 101011.
- 8. Elnokaly, A. and I. Keeling, *An Empirical Study Investigating the Impact of Micro-algal Technologies and their Application within Intelligent Building Fabrics*. Procedia Social and Behavioral Sciences, 2016. **216**: p. 712-723.
- 9. Wall, M., et al., *Achieving Solar Energy in Architecture-IEA SHC Task 41.* Energy Procedia, 2012. **30**: p. 1250-1260.
- 10. Visa, I., et al., *Facades Integrated Solar-thermal Collectors Challenges and Solutions*. Energy Procedia, 2017. **112**: p. 176-185.
- 11. Visa, I., A. Duta, and M. Moldovan, *Outdoor performance of a trapeze solar thermal collector for facades integration.* Renewable Energy, 2019. **137**: p. 37-44.
- 12. Cristofari, C., et al., *Building integration of solar thermal systems-example of a refurbishment of a church rectory.* Renewable Energy, 2019. **137**: p. 67-81.
- 13. Elguezabal, P., et al., *CFD model-based analysis and experimental assessment of key design parameters for an integrated unglazed metallic thermal collector façade.* Renewable Energy, 2020. **146**: p. 1766-1780.
- 14. Gunnewiek, L.H., E. Brundrett, and K.G.T. Hollands, *Flow distribution in unglazed transpired plate solar air heaters of large area*. Solar Energy, 1996. **58**(4): p. 227-237.
- 15. Gunnewiek, L.H., K.G.T. Hollands, and E. Brundrett, *Effect of wind on flow distribution in unglazed transpired-plate collectors*. Solar Energy, 2002. **72**(4): p. 317-325.
- 16. Van Decker, G.W.E., K.G.T. Hollands, and A.P. Brunger, *Heat-exchange relations for unglazed transpired solar collectors with circular holes on a square or triangular pitch.* Solar Energy, 2001. **71**(1): p. 33-45.
- 17. Gawlik, K.M. and C.F.J.J.S.E.E. Kutscher, *Wind heat loss from corrugated, transpired solar collectors.* 2002. **124**(3): p. 256-261.
- 18. Gawlik, K.M. and C.F. Kutscher. A numerical and experimental investigation of low-conductivity unglazed, transpired solar air heaters. in International Solar Energy Conference. 2002.
- 19. Mohamad, T., H. Moria, and F. Aldawi, *Radiation distribution uniformization by optimized halogen lamps arrangement for a solar simulator*. The Journal of Scientific and Engineering Research, 2016. **3**: p. 29-34.



- 20. Saini, P., et al., *Techno-economic analysis of an exhaust air heat pump system assisted by unglazed transpired solar collectors in a Swedish residential cluster.* Solar Energy, 2021. **224**: p. 966-983.
- 21. González-Martín, J., et al., *A state–of–the-art review on indoor air pollution and strategies for indoor air pollution control.* Chemosphere, 2021. **262**: p. 128376.
- 22. Ahmadi, Y., et al., *Recent advances in photocatalytic removal of airborne pathogens in air.* Science of The Total Environment, 2021. **794**: p. 148477.
- 23. Liu, S., M. Iten, and A. Shukla, *Numerical study on the performance of an air—Multiple PCMs unit for free cooling and ventilation.* Energy and Buildings, 2017. **151**: p. 520-533.
- 24. Rathore, P.K.S. and S.K. Shukla, *Enhanced thermophysical properties of organic PCM through shape stabilization for thermal energy storage in buildings: A state of the art review.* Energy and Buildings, 2021. **236**: p. 110799.
- 25. Yang, L., J.-n. Huang, and F. Zhou, *Thermophysical properties and applications of nanoenhanced PCMs: An update review.* Energy Conversion and Management, 2020. **214**: p. 112876.
- 26. Li, Z., Heat transfer during solidification of PCM layers with inclusion of nano-powders. International Communications in Heat and Mass Transfer, 2021. **127**: p. 105518.
- 27. Keshteli, A.N. and M. Sheikholeslami, *Influence of Al2O3 nanoparticle and Y-shaped fins on melting and solidification of paraffin.* Journal of Molecular Liquids, 2020. **314**: p. 113798.
- 28. Chen, S.-B., et al., *Combined effect of using porous media and nano-particle on melting performance of PCM filled enclosure with triangular double fins.* Case Studies in Thermal Engineering, 2021. **25**: p. 100939.
- 29. Sun, X., et al., Enhanced thermal energy storage of a paraffin-based phase change material (PCM) using nano carbons. Applied Thermal Engineering, 2020. **181**: p. 115992.
- 30. Xie, M., et al., *Improving the heat storage/release rate and photo-thermal conversion performance of an organic PCM/expanded graphite composite block.* Solar Energy Materials and Solar Cells, 2019. **201**: p. 110081.